

AD \_\_\_\_\_

Award Number: W81XWH-06-1-0196

TITLE: Contrast Agents for Micro-Computed Tomography of  
Microdamage in Bone

PRINCIPAL INVESTIGATOR: Ryan K. Roeder

CONTRACTING ORGANIZATION: University of Notre Dame  
Notre Dame, IN 46556

REPORT DATE: January 2008

TYPE OF REPORT: Annual

PREPARED FOR: U.S. Army Medical Research and Materiel Command  
Fort Detrick, Maryland 21702-5012

DISTRIBUTION STATEMENT: Approved for Public Release;  
Distribution Unlimited

The views, opinions and/or findings contained in this report are those of the author(s) and should not be construed as an official Department of the Army position, policy or decision unless so designated by other documentation.

| REPORT DOCUMENTATION PAGE   |             |                          |                            | Form Approved<br>OMB No. 0704-0188           |   |
|---|-------------|--------------------------|----------------------------|--|---|
| Public reporting burden for this collection of information is estimated to average 1 hour per response, including the time for reviewing instructions, searching existing data sources, gathering and maintaining the data needed, and completing and reviewing this collection of information. Send comments regarding this burden estimate or any other aspect of this collection of information, including suggestions for reducing this burden to Department of Defense, Washington Headquarters Services, Directorate for Information Operations and Reports (0704-0188), 1215 Jefferson Davis Highway, Suite 1204, Arlington, VA 22202-4302. Respondents should be aware that notwithstanding any other provision of law, no person shall be subject to any penalty for failing to comply with a collection of information if it does not display a currently valid OMB control number. <b>PLEASE DO NOT RETURN YOUR FORM TO THE ABOVE ADDRESS.</b>   |             |                          |                            |  |   |
| 1. REPORT DATE<br>31-01-2008  |             | 2. REPORT TYPE<br>Annual |                            | 3. DATES COVERED<br>1 JAN 2006 - 31 DEC 2007 |   |
| 4. TITLE AND SUBTITLE<br>Contrast Agents for Micro-Computed Tomography of Microdamage in Bone   |             |                          |                            | 5a. CONTRACT NUMBER                          |   |
|   |             |                          |                            | 5b. GRANT NUMBER<br>W81XWH-06-1-0196         |   |
|   |             |                          |                            | 5c. PROGRAM ELEMENT NUMBER                   |   |
| 6. AUTHOR(S)<br>Ryan K. Roeder<br><br>Email: rroeder@nd.edu   |             |                          |                            | 5d. PROJECT NUMBER                           |   |
|   |             |                          |                            | 5e. TASK NUMBER                              |   |
|   |             |                          |                            | 5f. WORK UNIT NUMBER                         |   |
| 7. PERFORMING ORGANIZATION NAME(S) AND ADDRESS(ES)<br><br>University of Notre Dame<br>Notre Dame, IN 46556  |             |                          |                            | 8. PERFORMING ORGANIZATION REPORT NUMBER     |   |
|   |             |                          |                            |  |   |
| 9. SPONSORING / MONITORING AGENCY NAME(S) AND ADDRESS(ES)<br>U.S. Army Medical Research and Materiel Command<br>Fort Detrick, Maryland 21702-5012   |             |                          |                            | 10. SPONSOR/MONITOR'S ACRONYM(S)             |   |
|   |             |                          |                            | 11. SPONSOR/MONITOR'S REPORT NUMBER(S)       |   |
| 12. DISTRIBUTION / AVAILABILITY STATEMENT<br>Approved for Public Release; Distribution Unlimited  |             |                          |                            |  |   |
| 13. SUPPLEMENTARY NOTES   |             |                          |                            |  |   |
| 14. ABSTRACT<br>Novel methods have been developed for detecting damaged bone tissue using micro-computed tomography (micro-CT) and contrast agents with higher x-ray attenuation than bone. The ability to detect the presence, and to a limited extent the morphology, of microdamage in cortical and trabecular bone using micro-CT was demonstrated using a barium sulfate (BaSO <sub>4</sub> ) stain. Gold nanoparticles (Au NPs) were prepared and functionalized with L-glutamic acid for chelating calcium in damaged bone tissue. The functionalized Au NP contrast agent exhibited damage-specificity confirmed by optical, electron and AFM imaging. Functionalized Au NPs were also conjugated with fluorescein to produce a dual contrast agent suitable for both fluorescent microscopy and micro-CT. The small size ( 40 nm) and colloidal stability of functionalized Au NP solutions enabled the contrast agent to readily diffuse into bone tissue, which suggests that the contrast agent is deliverable. |             |                          |                            |  |   |
| 15. SUBJECT TERMS<br>Bone; Microdamage; Computed Tomography; Contrast Agents; Barium Sulfate; Gold; Nanoparticles   |             |                          |                            |  |   |
| 16. SECURITY CLASSIFICATION OF:   |             |                          | 17. LIMITATION OF ABSTRACT | 18. NUMBER OF PAGES                          | 19a. NAME OF RESPONSIBLE PERSON           |
| a. REPORT   | b. ABSTRACT | c. THIS PAGE             |                            |  | USAMRMC                                   |
| U   | U           | U                        | UU                         | 36   | 19b. TELEPHONE NUMBER (include area code) |

## Table of Contents

|                                   | <u>Page</u> |
|-----------------------------------|-------------|
| Introduction.....                 | 4           |
| Body.....                         | 4           |
| Key Research Accomplishments..... | 9           |
| Reportable Outcomes.....          | 9           |
| Conclusion.....                   | 11          |
| References.....                   | 11          |
| Appendices.....                   | 12          |

## INTRODUCTION

Accumulation of microdamage in bone tissue can lead to an increased risk of fracture, including stress fractures in active individuals and fragility fractures in the elderly. Current methods for detecting microdamage are inherently invasive, destructive, tedious and two-dimensional. These limitations inhibit evaluating the effects of microdamage on whole bone strength and prohibit detecting microdamage *in vivo*. Therefore, we are investigating novel methods for detecting microdamage in bone using micro-computed tomography (micro-CT) and contrast agents with higher x-ray attenuation than bone. For proof-of-concept, the presence, spatial variation and accumulation of microdamage in cortical and trabecular bone specimens was nondestructively detected using micro-CT after staining with barium sulfate. However, specimens were stained *in vitro* via a precipitation reaction which was non-specific to damage and not biocompatible. Therefore, we are currently investigating the synthesis and functionalization of gold and barium sulfate nanoparticles for deliverable, damage-specific contrast agents. The objectives of the research are to 1) develop damage-specific contrast agents, with greater x-ray attenuation than bone, for micro-computed tomography (micro-CT) of microdamage; 2) evaluate the x-ray attenuation, deliverability and specificity of contrast agent formulations; and, 3) quantify the effects of the contrast agent on micro-CT images in damaged and undamaged bone, and correlate the measurements to traditional measures of microdamage. Research progress in each of the specific aims is discussed below.

## BODY

**Task 1:** Develop damage-specific contrast agents, with greater x-ray attenuation than bone, for micro-computed tomography (micro-CT) of microdamage (Months 1-24).

*Aim 1.1 Synthesize barium sulfate ( $\text{BaSO}_4$ ) nanoparticles with a mean size less than 10 nm (Months 1-6).*

$\text{BaSO}_4$  nanoparticles were readily synthesized using a microemulsion technique. The nanoparticles exhibited uniform size and shape, with a mean size less than 10 nm as characterized by DLS and TEM (Fig. 1). For a detailed description, see Meagher *et al.* (2007) in the Appendices.

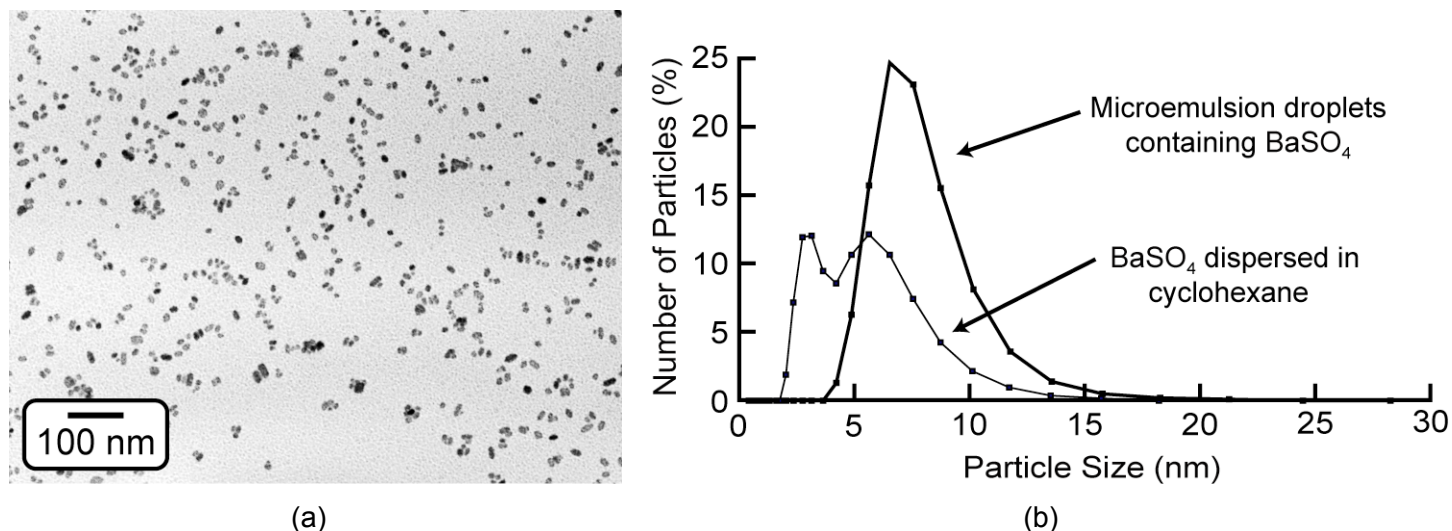


**Fig. 1.** (a) TEM micrograph showing the size and morphology of as-prepared  $\text{BaSO}_4$  nanoparticles. (b) Particle size distribution measured by DLS (Malvern Zetasizer Nano-ZS).

In order to circumvent challenges stabilizing and functionalizing  $\text{BaSO}_4$  nanoparticles (described below), gold nanoparticles (Au NPs) were also prepared using the citrate reduction method. As-prepared Au NPs exhibited uniform size and shape, with a mean size of 15 or 40 nm, depending on synthesis conditions, as characterized by DLS and TEM (Fig. 2). For a detailed description, see Zhang *et al.* (2007) in the Appendices.

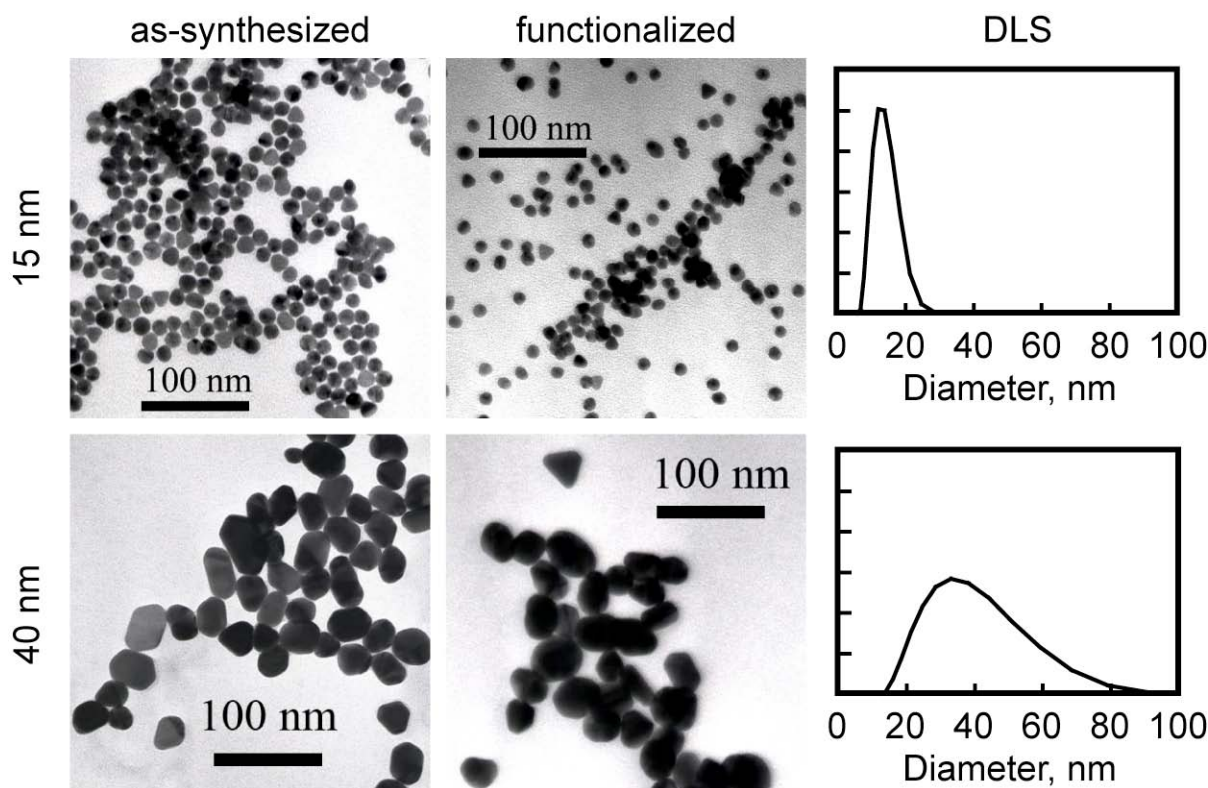


**Fig. 2.** TEM micrographs, and particle size distributions measured by DLS (Malvern Zetasizer Nano-ZS), showing the size and morphology of as-synthesized and functionalized Au NPs.

*Aim 1.2 Stabilize and functionalize colloidal dispersions of BaSO<sub>4</sub> nanoparticles with (macro)molecules containing multiple carboxy, hydroxyl and/or phosphonate ligands able to simultaneously bind with both the nanoparticle and calcium ions exposed on surfaces created by microdamage in bone (Months 1-24).*

The colloidal stability and functionalization of BaSO<sub>4</sub> nanoparticles has provided a greater challenge than anticipated. BaSO<sub>4</sub> nanoparticles were dispersed in non-aqueous solvents, but readily agglomerated once removed from the stabilizing environment of the microemulsion and redispersed in polar solvents such as water. The zeta potential of BaSO<sub>4</sub> nanoparticles was measured (Malvern Zetasizer Nano-ZS) from neutral to basic pH through titration with sodium hydroxide (NaOH). Despite a zeta potential above 25 mV for pH ≥ 8, which is typically reported to produce stable dispersions, the particles continued to agglomerate. Furthermore, the surface chemistry of BaSO<sub>4</sub> was not amenable to typical approaches of surface functionalization. Ongoing efforts are investigating the use of dextran coatings to stabilize BaSO<sub>4</sub> nanoparticles and provide a chemistry amenable to functionalization with carboxy ligands. Dextran coatings have been used to stabilize superparamagnetic iron oxide nanoparticles used as an MRI contrast agent [1-3]. For a detailed description, see Meagher *et al.* (2007) in the Appendices.

In contrast to the challenges encountered with BaSO<sub>4</sub> nanoparticles, Au NPs were readily functionalized with L-glutamic acid, presenting carboxy ligands to chelate calcium in damaged bone tissue (Fig. 3). The particle size (Fig. 2) and the plasmon band for Au NPs in UV-Vis spectroscopy was unchanged after functionalization indicating that the nanoparticles remained dispersed. For a detailed description, see Zhang *et al.* (2007) in the Appendices.

Principal Investigator: Roeder, Ryan K.

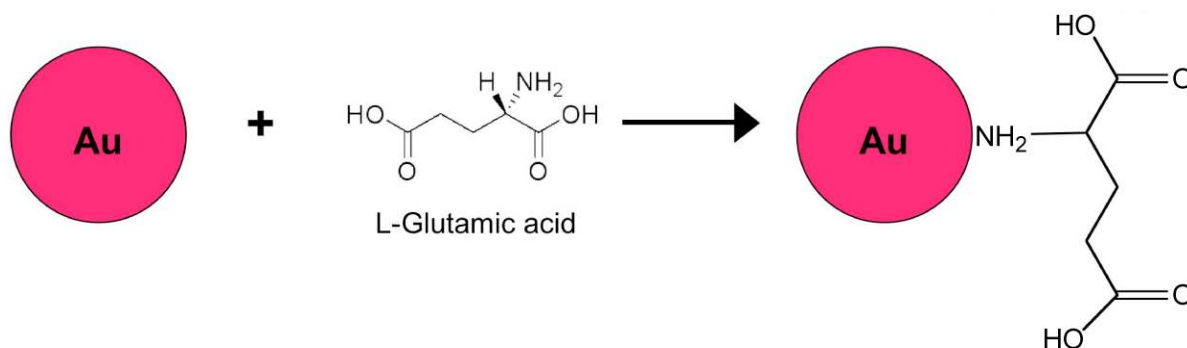


**Fig. 3.** Schematic diagram showing functionalization of Au NPs with L-glutamic acid.

*Aim 1.3 Synthesize iodinated molecules containing multiple phosphonate ligands with a high binding affinity for calcium ions exposed on surfaces created by microdamage in bone (Months 1-24).*

This aim involved synthetic chemistry beyond the skill set of the post-doctoral research associate that was hired, who was skilled primarily in inorganic and surface chemistry. Furthermore, since the time this proposal was submitted, another research group in Ireland has prepared iodinated molecules functionalized with carboxy ligands and their results suggest that the iodinated molecules were readily washed away from damaged tissue and did not provide sufficient x-ray attenuation relative to bone tissue [4,5]. Therefore, the PI has formed a new collaboration with Dr. Marya Lieberman in the Department of Chemistry at Notre Dame to investigate routes of functionalizing Au NPs with phosphate and phosphonate ligands. Results are expected in the next year of the grant.

**Task 2:** Evaluate the x-ray attenuation, deliverability and specificity of contrast agent formulations (Months 6-36).

*Aim 2.1 Measure the particle size and/or molecular weight of the contrast agent (Months 1-12).*

See results reported under Aim 1.1.

*Aim 2.2 Measure the mass attenuation and partial volume effect of known concentrations of the contrast agents on micro-CT images (Months 7-18).*

Our commercial micro-CT scanner (ScanCo  $\mu$ CT-80,  $\approx 10$   $\mu$ m resolution) has thus far been unable to detect the Au NPs at the small size and low concentration required for a deliverable contrast agent. We are in the process of investigating 1) improved image processing, 2) the detection limit of our scanner, 3) a theoretical model for the detection limit for gold in bone [6], and 4) the use of higher resolution instruments. Preliminary studies with computed tomography using high energy synchrotron radiation at Argonne National Laboratory have also been discouraging. The use of this facility enables the highest resolution available ( $\approx 100$  nm) and the x-ray energy to be tailored to maximize the difference in attenuation between bone and gold at the  $\approx 11$  keV absorption edge of gold, but not the larger absorption edge at  $\approx 80$  keV (Fig. 4). We have since submitted a proposal to Argonne National Laboratory, which is a short 2-3 hour drive from Notre Dame, for formalized beam time in order to determine the detection limits of gold in bone. The full proposal is included in the Appendices.

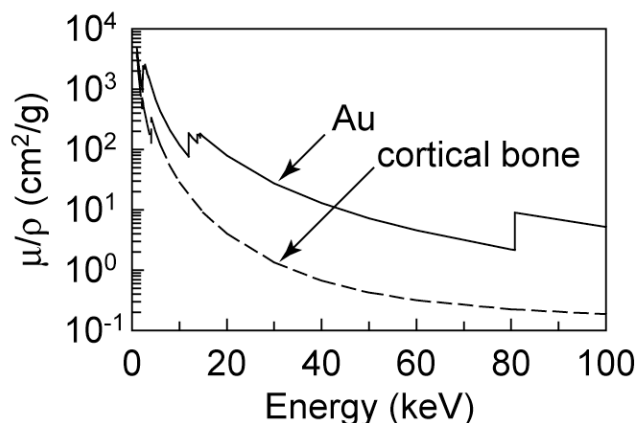


**Fig. 4.** The mass attenuation coefficient of gold and cortical bone versus the energy of the x-ray source. Data was adapted from the NIST X-ray attenuation databases [7].



In summary, while we remain hopeful in our current efforts, we cannot rule out that a possible negative result from this project will be that deliverable, damage-specific contrast agents are not able to be detected in bone tissue using current, commercially available CT imaging technology. Note that Au NPs have been used successfully as a vascular contrast agent [8,9] and recently commercialized (AuroVist™, Nanoprobe); however, the relative difference in attenuation between soft tissue and gold is much higher than between calcified tissue and gold.

*Aim 2.3 Determine the stability of the contrast agent in phosphate buffered saline, simulated body fluid (SBF) and/or fetal bovine serum (FBS) (Months 13-24).*

Stability has been determined in water as described under Aim 1.2. Studies for the stability of the Au NP contrast agent in the presence of physiologically relevant counter-ions and proteins are ongoing, and are not expected to be problematic [8].

*Aim 2.4 Validate the specificity of the contrast agent for microdamage using machined surfaces of bovine cortical bone (Months 19-30).*

The functionalized Au NP contrast agent exhibited damage-specificity. Machined surfaces of bovine cortical bone were first stained with calcein to mask machining damage. Controlled surface damage was subsequently created by scratching the surfaces with a scalpel. Specimens were then immersed in functionalized Au NP solutions to stain the damage. The specificity of the contrast agent for damage (surface scratches) was readily apparent to the naked eye due to the natural color of the Au NPs (Fig. 5a). The specificity was further confirmed at high resolution with SEM using backscattered electron imaging (BEI) (Fig. 5b) and AFM (Fig. 6). These are the most significant results of the project thus far and the subject of manuscripts in preparation.

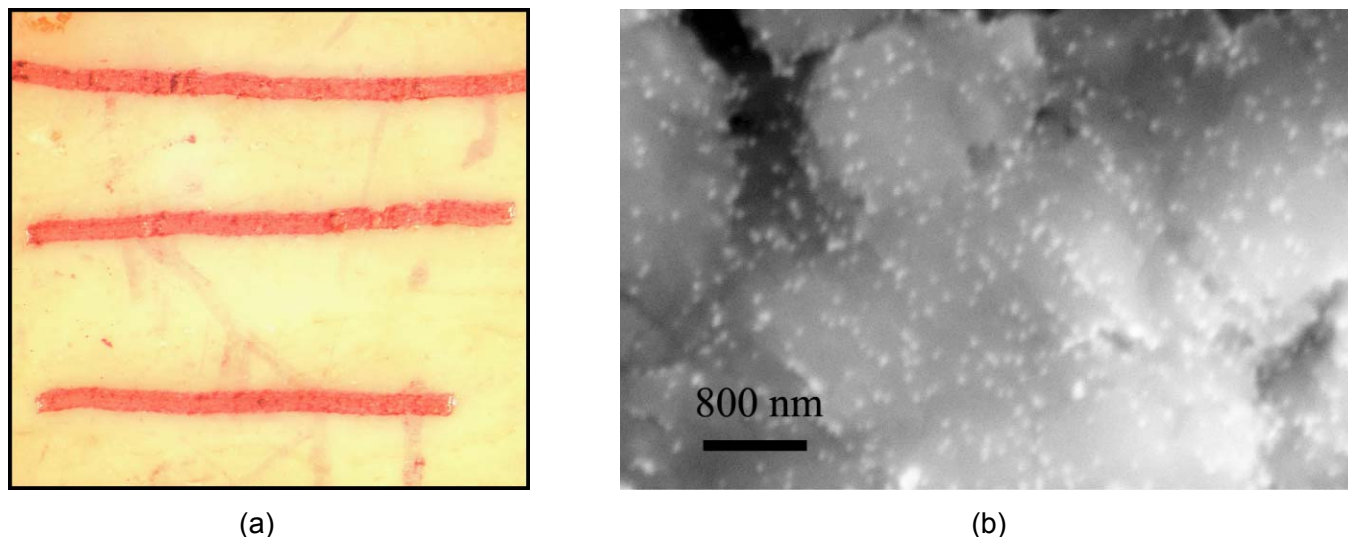


**Fig. 5.** (a) Optical micrograph showing scratches on the surface of a bone specimen stained by 15 nm Au NPs (red). The width of the specimen is 7 mm. (b) SEM micrograph using BEI confirming the presence of Au NPs (bright dots) on the surface of the scratch.

*Aim 2.5 Measure the diffusivity of the contrast agent into both cortical and trabecular bone tissue (Months 25-36).*

In order to most easily track the diffusion of Au NPs in bone tissue, as-prepared Au NPs were conjugated with a fluorophore, fluorescein (Fig. 7a). UV-Vis spectroscopy showed that the Au NPs remained dispersed and fluorescein retained its characteristic epifluorescence (Fig. 7b). Therefore, we have prepared a dual contrast agent able to be imaged by x-ray and epifluorescence. A scratch test similar to that described in Aim 2.4 showed that the dual contrast agent exhibited specificity for damage (Fig. 7c). Preliminary diffusivity experiments have shown that the contrast agent diffuses readily into cortical bone tissue.

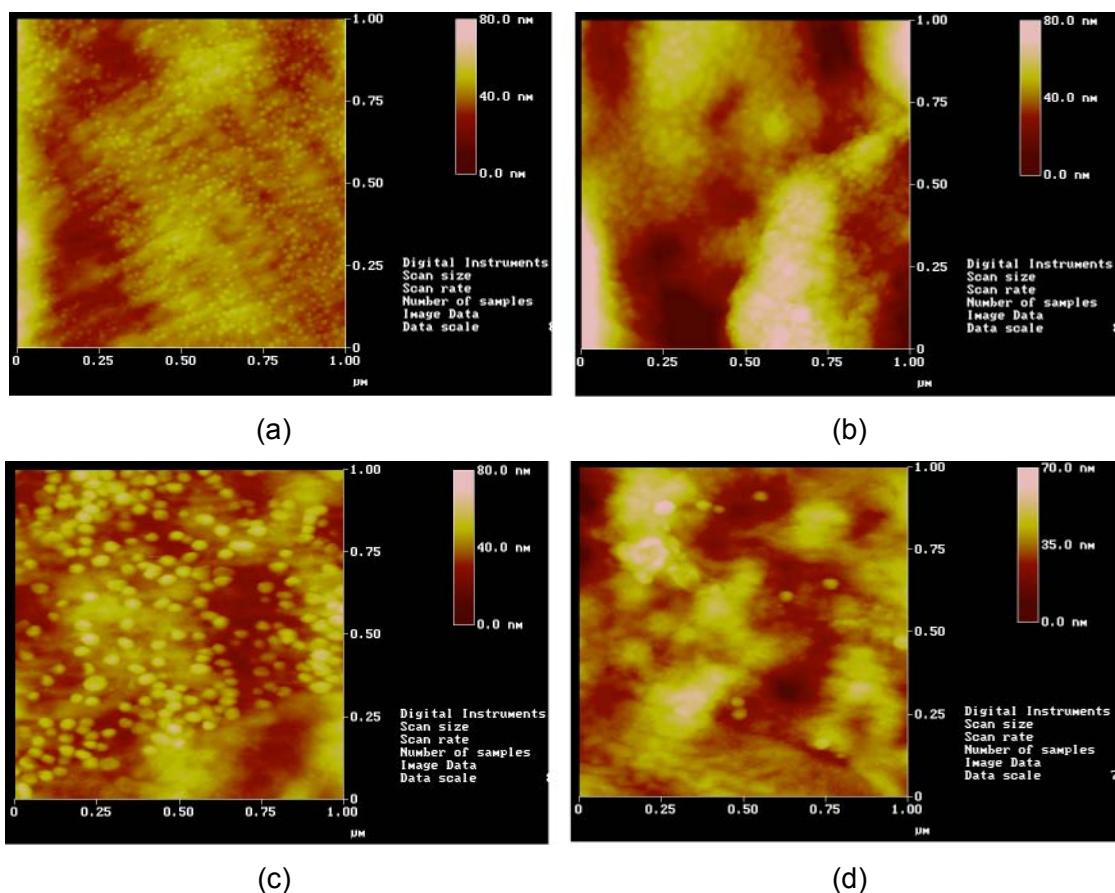


**Fig. 6.** AFM images showing the specificity of the functionalized Au NP contrast agent for the surface damage of the scratch (a,c) versus tissue away from the scratch for 15 nm (a,b) and 40 nm (c,d).

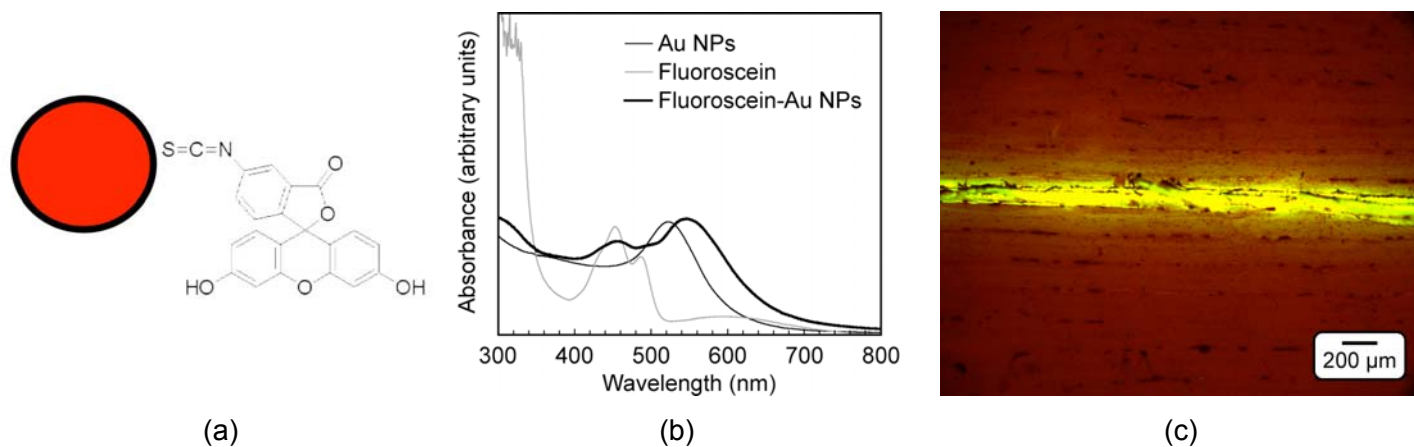


**Fig. 7.** (a) Schematic diagram showing functionalization of Au NPs with fluoroscein. (b) UV-Vis spectra measured for as-prepared Au NPs, fluoroscein and Au NPs conjugated with fluoroscein. (c) UV light micrograph showing a scratch on the surface of a bone specimen stained by Au NPs conjugated with fluoroscein (yellow-green).



Principal Investigator: Roeder, Ryan K.

**Task 3:** Quantify the effects of the contrast agent on micro-CT images in damaged and undamaged bone, and correlate the measurements to traditional measures of microdamage (Months 25-48).

*Aim 3.1 Quantify the measured mass attenuation in rectangular notched and un-notched human cortical bone bending specimens, and correlate micro-CT measurements to the microdamage density measured by fluorescent staining and microscopy (Months 25-42).*

*Aim 3.2 Quantify locations and levels of microdamage in trabecular bone subjected to torsional loading, and validate the measurements by comparing to fluorescent staining and microscopy (Months 37-48).*

*Aim 3.3 Quantify microdamage in whole rat femurs subjected to bending (Months 37-48).*

We are preparing to begin studies for Aims 3.1-3.3. Note that the inability to image the functionalized Au NP contrast agent using our micro-CT may require that these studies be conducted using the fluorescein-Au NP contrast agent with fluorescent microscopy and/or the BaSO<sub>4</sub> stain, which is not damage-specific, with micro-CT. In the former case, we will be demonstrating the utility and validating the new damage-specific nanoparticle contrast agent in the event that new, improved CT technology were to become available. In the latter case, validation of the BaSO<sub>4</sub> stain, while not damage-specific or biocompatible, would still enable nondestructive imaging of microdamage by micro-CT, which would provide a useful new technique for the scientific study of microdamage in bone. For a detailed description of the the BaSO<sub>4</sub> stain, see Leng *et al.* (2008) and Wang *et al.* (2007) in the Appendices.

## **Timeline**

Progress toward the above Tasks and Aims is generally on schedule, given a three-six month window from the official award date (1/1/06) until the time key personnel (e.g., the postdoc and GAs) were in place.

## **KEY RESEARCH ACCOMPLISHMENTS**

- The ability to detect the presence, and to a limited extent the morphology, of microdamage in cortical and trabecular bone using micro-CT was demonstrated using a barium sulfate (BaSO<sub>4</sub>) stain.
- Gold nanoparticles (Au NPs) were prepared ( $\leq 40$  nm) and functionalized with L-glutamic acid for chelating calcium in damaged bone tissue.
- The functionalized Au NP contrast agent exhibited damage-specificity confirmed by optical, electron and AFM imaging.
- Functionalized Au NPs were also conjugated with fluorescein to produce a dual contrast agent suitable for both fluorescent microscopy and micro-CT.
- The small size ( $\leq 40$  nm) and colloidal stability of functionalized Au NP solutions enabled the contrast agent to readily diffuse into bone tissue, which suggests that the contrast agent is deliverable.

## **REPORTABLE OUTCOMES**

### Journal Publications

Z. Zhang, R.D. Ross and R.K. Roeder, "Functionalized Gold Nanoparticles as a Damage Specific Contrast Agent for Bone," in preparation.

M.J. Meagher, Z. Zhang, and R.K. Roeder, "Precipitation of Barium Sulfate Nanoparticles Using Microemulsions," in preparation.

M.D. Landrigan and R.K. Roeder, "Systematic error in the measure of microdamage by modulus degradation during four-point bending fatigue of cortical bone," *J. Biomechanics*, submitted.

Principal Investigator: Roeder, Ryan K.

H. Leng, X. Wang, R.D. Ross, G.L. Niebur and R.K. Roeder, "Micro-computed tomography of fatigue microdamage in cortical bone using a barium sulfate contrast agent," *J. Mech. Behav. Biomed. Mater.*, **1** [1] 68-75 (2008).

X. Wang, D.B. Masse, H. Leng, K.P. Hess, R.D. Ross, R.K. Roeder and G.L. Niebur, "Detection of trabecular bone microdamage by micro-computed tomography," *J. Biomechanics*, **40** [15] 3397-3403 (2007).

#### Conference Proceedings and Abstracts

R.D. Ross, Z. Zhang and R.K. Roeder, "Functionalized Gold Nanoparticles as an X-ray Contrast Agent for Bone Microdamage," *2008 TMS Annual Meeting*, New Orleans, LA (2008).

R.K. Roeder, Z. Zhang, R.D. Ross, M.D. Landrigan and H. Leng, "Noninvasive Imaging of Microdamage in Bone," *Materials Science and Technology 2007 (MS&T '07)*, Detroit, MI (2007). Invited.

M.D. Landrigan and R.K. Roeder, "Systematic Error in the Measure of Microdamage by Modulus Degradation During Four-Point Bending Fatigue," *Proc. of the 2007 Summer Bioengineering Conference (ASME)*, Keystone, CO, 175238 (2007). Honorable mention in the Ph.D. Student Paper Competition – Poster Presentation, Solid Mechanics, Design and Rehabilitation.

Z. Zhang, R.D. Ross and R.K. Roeder, "Functionalized Gold Nanoparticles as a Damage Specific Contrast Agent for Bone," *Trans. of the 33rd Annual Meeting of the Society for Biomaterials*, Chicago, IL, **30**, 93 (2007).

M.J. Meagher, Z. Zhang, and R.K. Roeder, "Precipitation of a Barium Sulfate Nanoparticle Contrast Agent Using Microemulsions," *2007 TMS Annual Meeting*, Orlando, FL (2007).

#### Personnel Report (including new degrees and employment)

| Name            | Role    | Period     | % Effort | New Degrees | Current Position                     |
|-----------------|---------|------------|----------|-------------|--------------------------------------|
| Ryan K. Roeder  | PI      | 1/06-      | 8        | n/a         | promoted to Assoc. Prof. with tenure |
| Glen L. Niebur  | co-PI   | 1/06-      | 8        | n/a         | promoted to Assoc. Prof. with tenure |
| Zhenyuan Zhang  | Postdoc | 6/06-12/07 | 100      | n/a         | Research Scientist, Sandia Nat. Lab. |
| Huijie Leng     | GA      | 1/06-10/06 | 100      | PhD (2006)  | Postdoc, UTSA                        |
| Matt Landrigan  | GA      | 6/06-      | 100      | MS (2007)   | pursuing PhD at Notre Dame           |
| Ryan Ross       | GA      | 8/06-      | 100      |             | pursuing PhD at Notre Dame           |
| Jackie Garrison | GA      | 1/08-      | 100      |             | pursuing PhD at Notre Dame           |
| Matt Meagher    | UG RA   | 6/06-8/06  | 100      |             | pursuing BS at Notre Dame            |
| Paul Baranay    | UG RA   | 6/07-8/07  | 100      |             | pursuing BS at MIT                   |
| Carl Berasi     | UG RA   | 1/07-      | unpaid   |             | pursuing BS at Notre Dame            |
| Erin Heck       | UG RA   | 1/07-5/07  | unpaid   |             | pursuing BS at Notre Dame            |
| Jimmy Buffi     | UG RA   | 8/07-      | unpaid   |             | pursuing BS at Notre Dame            |
| Bridget Leone   | UG RA   | 1/08-      | unpaid   |             | pursuing BS at Notre Dame            |

Note that GA = graduate assistant and UG RA = undergraduate research assistant.

## CONCLUSION

A biocompatible, deliverable, damage-specific contrast agent with greater x-ray attenuation than bone would enable non-destructive, three-dimensional and non-invasive (*in vivo*) imaging of microdamage in bone. Such a contrast agent would have the potential to enable clinical assessment of bone quality and damage accumulation, and scientific study of damage processes *in situ*. The results of this project to date, suggest that this ambitious goal may require some near term compromise. A functionalized gold nanoparticle (Au NP) contrast agent was prepared for biocompatibility, deliverability and damage-specificity. Preliminary results have demonstrated damage specificity and deliverability. However, these requirements limited the contrast agent to a size and concentration that has not yet been able to be detected in bone using current, commercially available micro-CT technology. Therefore, the results of this work so far suggest that the ambitious goal of non-invasive (*in vivo*) imaging of microdamage in bone would be feasible, *if* new technology were to significantly improve the detection limits and radiation dosage of CT instruments.

On the other hand, an x-ray contrast agent “merely” able to label microdamage in bone (though not biocompatible, deliverable or damage-specific) will still enable non-destructive and three-dimensional (though not *in vivo*) imaging of microdamage in bone. Such a contrast agent will still have the potential to improve the scientific study of microdamage accumulation, as existing methods of damage detection are inherently destructive, two-dimensional and tedious. In light of this, and unless a breakthrough is made during the next six months, including our proposed beam time at the Argonne National Laboratory, we propose that Task 3 of the project be modified to include investigation and validation of the barium sulfate (BaSO<sub>4</sub>) stain, which is readily imaged by current, commercially available micro-CT technology. The BaSO<sub>4</sub> stain would be used for Task 3 in place of, or in addition to, the damage-specific nanoparticle contrast agents. Remaining work on Tasks 1 and 2 will continue with the new damage-specific nanoparticle contrast agents that have been developed.

## REFERENCES

1. M. Lewin, N. Carlesso, C-H. Tung, X-W. Tang, D. Cory, D.T. Scadden and R. Weissleder, “Tat peptide-derivatized magnetic nanoparticles allow in vivo tracking and recovery of progenitor cells,” *Nature Biotech.*, **18** [4] 410-414 (2000).
2. M. Zhao, D.A. Beauregard, L. Loizou, B. Davletov and K.M. Brindle, “Non-invasive detection of apoptosis using magnetic resonance imaging and a targeted contrast agent,” *Nature Med.*, **7** [11] 1241-1244 (2001).
3. E.A. Schellenberger, A. Bogdanov Jr., D. Högemann, J. Tait, R. Weissleder and L. Josephson, “Annexin V-CLIO: A Nanoparticle for Detecting Apoptosis by MRI,” *Mol. Imaging*, **1** [2] 102-107 (2002).
4. R. Parkesh, T. C. Lee, T. Gunnlaugsson and W. Gowin, “Microdamage in bone: Surface analysis and radiological detection,” *J. Biomechanics*, **39** 1552-1556 (2006).
5. R. Parkesh, S. Mohsin, T. C. Lee and T. Gunnlaugsson, “Histological, Spectroscopic, and Surface Analysis of Microdamage in Bone: Toward Real-Time Analysis Using Fluorescent Sensors,” *Chem. Mater.*, **19** 1656-1663 (2007).
6. K. Kouris, N.M. Spyrou and D.F. Jackson, “Minimum Detectable Quantities of Elements and Compounds in a Biological Matrix,” *Nuclear Instr. Methods*, **187**, 539-545 (1981).
7. J.H. Hubbell and S.M. Setzer, *Tables of X-Ray Mass Attenuation Coefficients and Mass Energy-Absorption Coefficients* (version 1.4). [Online] Available: <http://physics.nist.gov/xaamdi> [2008, January 29]. National Institute of Standards and Technology, Gaithersburg, MD, 2004.
8. J.F. Hainfield, D.N. Slatkin and H.M. Smilowitz, “The use of gold nanoparticles to enhance radiotherapy,” *Phys. Med. Biol.*, **49**, N309-N315 (2004).
9. J.F. Hainfield, D.N. Slatkin, T.M. Focella and H.M. Smilowitz, “Gold nanoparticles: an new X-ray contrast agent,” *Brit. J. Radiol.*, **79** [3] 248-253 (2006).

## APPENDICES

Attached reprints include:

H. Leng, X. Wang, R.D. Ross, G.L. Niebur and R.K. Roeder, "Micro-computed tomography of fatigue microdamage in cortical bone using a barium sulfate contrast agent," *J. Mech. Behav. Biomed. Mater.*, **1** [1] 68-75 (2008).

X. Wang, D.B. Masse, H. Leng, K.P. Hess, R.D. Ross, R.K. Roeder and G.L. Niebur, "Detection of trabecular bone microdamage by micro-computed tomography," *J. Biomechanics*, **40** [15] 3397-3403 (2007).

R.D. Ross, Z. Zhang and R.K. Roeder, "Functionalized Gold Nanoparticles as an X-ray Contrast Agent for Bone Microdamage," *2008 TMS Annual Meeting*, New Orleans, LA (2008).

M.D. Landrigan and R.K. Roeder, "Systematic Error in the Measure of Microdamage by Modulus Degradation During Four-Point Bending Fatigue," *Proc. of the 2007 Summer Bioengineering Conference (ASME)*, Keystone, CO, 175238 (2007).

Z. Zhang, R.D. Ross and R.K. Roeder, "Functionalized Gold Nanoparticles as a Damage Specific Contrast Agent for Bone," *Trans. of the 33rd Annual Meeting of the Society for Biomaterials*, Chicago, IL, **30**, 93 (2007).

M.J. Meagher, Z. Zhang, and R.K. Roeder, "Precipitation of a Barium Sulfate Nanoparticle Contrast Agent Using Microemulsions," *2007 TMS Annual Meeting*, Orlando, FL (2007).

R.K. Roeder, R.D. Ross and Z. Zhang, "The detection limit of gold nanoparticles in x-ray tomography," Proposal GUP-8931, Argonne National Laboratory, submitted November, 2007.

available at [www.sciencedirect.com](http://www.sciencedirect.com)journal homepage: [www.elsevier.com/locate/jmbbm](http://www.elsevier.com/locate/jmbbm)

## Research paper

# Micro-computed tomography of fatigue microdamage in cortical bone using a barium sulfate contrast agent

Huijie Leng<sup>1</sup>, Xiang Wang<sup>2</sup>, Ryan D. Ross, Glen L. Niebur, Ryan K. Roeder\*

Department of Aerospace and Mechanical Engineering, The University of Notre Dame, Notre Dame, IN 46556, United States

## ARTICLE INFO

## Article history:

Received 4 May 2007

Received in revised form

31 May 2007

Accepted 4 June 2007

Published online 31 July 2007

## Keywords:

Fatigue microdamage

Cortical bone

Micro-computed tomography

Contrast agents

Barium sulfate

## ABSTRACT

Accumulation of microdamage during fatigue can lead to increased fracture susceptibility in bone. Current techniques for imaging microdamage in bone are inherently destructive and two-dimensional. Therefore, the objective of this study was to image the accumulation of fatigue microdamage in cortical bone using micro-computed tomography (micro-CT) with a barium sulfate ( $\text{BaSO}_4$ ) contrast agent. Two symmetric notches were machined on the tensile surface of bovine cortical bone beams in order to generate damage ahead of the stress concentrations during four-point bending fatigue. Specimens were loaded to a specified number of cycles or until one notch fractured, such that the other notch exhibited the accumulation of microdamage prior to fracture. Microdamage ahead of the notch was stained *in vitro* by precipitation of  $\text{BaSO}_4$  and imaged using micro-CT. Reconstructed images showed a distinct region of bright voxels around the notch tip or along propagating cracks due to the presence of  $\text{BaSO}_4$ , which was verified by backscattered electron imaging and energy dispersive spectroscopy. The shape of the stained region ahead of the notch tip was consistent with principal strain contours calculated by finite element analysis. The relative volume of the stained region was correlated with the number of loading cycles by non-linear regression using a power law. This study demonstrates new methods for the non-destructive and three-dimensional detection of fatigue microdamage accumulation in cortical bone *in vitro*, which may be useful to gain further understanding into the role of microdamage in bone fragility.

© 2007 Elsevier Ltd. All rights reserved.

## 1. Introduction

Healthy bone is crucial to overall human health. Bone provides structural support for the body, protects soft tissues and organs, produces red blood cells, stores essential minerals and transmits muscular forces during movement (Jee, 2001). Microdamage accumulates in bone tissue *in vivo*

due to repetitive loading and is observed in the form of microcracks or diffuse damage (Burr et al., 1997; Martin, 2003). *In vitro* studies have shown that microdamage accumulation has a detrimental effect on the mechanical properties of cortical bone (Jepsen and Davy, 1997; Schaffler et al., 1989). However, *in vivo*, microdamage is repaired by, and may signal, bone remodeling (Burr et al., 1985; Martin, 2003; Martin and

\* Corresponding author. Tel.: +1 574 631 7003; fax: +1 574 631 2144.

E-mail address: [rroeder@nd.edu](mailto:rroeder@nd.edu) (R.K. Roeder).

<sup>1</sup> Current Address: Department of Mechanical Engineering, University of Texas at San Antonio, San Antonio, TX 78249, United States.

<sup>2</sup> Current Address: Department of Orthopaedic Surgery, University of California, Davis, Sacramento, CA 95817, United States.

Burr, 1982; Mori and Burr, 1993). Thus, excessive accumulation of microdamage prior to remodeling can lead to increased fracture susceptibility. However, the role of microdamage in clinical bone fragility is not yet well understood, in part due to limited capabilities for imaging and measuring microdamage accumulation both *in vivo* and *in vitro*.

Current imaging techniques, such as ultraviolet light microscopy using fluorescent stains or chelating agents (Burr and Stafford, 1990; Lee et al., 2000; O'Brien et al., 2002, 2005), backscattered electron imaging (BEI) using a lead-uranyl acetate stain (Schaffler et al., 1994), laser scanning confocal microscopy (LSCM) using fluorescent stains (O'Brien et al., 2000; Zioupos and Currey, 1994) and serial imaging using fluorescent stains (O'Brien et al., 2000), require the preparation of many histologic sections which are inherently destructive and two-dimensional. LSCM provides limited depth of field for three-dimensional (3D) imaging of labeled microdamage, but the sample preparation is destructive and the depth of field is not sufficient to image whole microcracks and tissue architecture.

A non-destructive and 3D imaging technique would enable measurement of the spatial density of microdamage accumulation, which could be correlated to local variations in mechanical loading, bone mineral density (BMD) or microarchitecture. Therefore, recent studies have begun to investigate non-invasive, 3D imaging techniques. Positron emission tomography (PET) was used to image microdamage *in vivo* with a sodium fluoride ( $\text{Na}^{18}\text{F}$ ) contrast agent (Li et al., 2005; Silva et al., 2006). Micro-computed tomography (micro-CT) was used to detect microdamage *in vitro* with lead sulfide (PbS) (Leng et al., 2005), barium sulfate ( $\text{BaSO}_4$ ) (Wang et al., *in press*) or iodinated (Parkesh et al., 2006, 2007) contrast agents. In particular,  $\text{BaSO}_4$  was proposed as a more benign alternative to lead-based stains.  $\text{BaSO}_4$  was also considered a logical choice for a contrast agent with potential for future use *in vivo* due to high x-ray attenuation and reasonable biocompatibility.  $\text{BaSO}_4$  is currently used clinically as a contrast agent for gastrointestinal radiography (Skucas, 1989) and as a radiopacifier in polymethylmethacrylate bone cement (Lewis, 1997).

The objective of this study was to non-destructively and three-dimensionally image microdamage accumulation in cortical bone *in vitro* using micro-CT with a  $\text{BaSO}_4$  contrast agent. The  $\text{BaSO}_4$  stain employed in this study was previously used to label microdamage *in vitro* in trabecular bone specimens that were damaged by an overload (Wang et al., *in press*). In this study, similar methods were used to detect the progressive accumulation of fatigue microdamage ahead of a notch in cortical bone specimens.

## 2. Materials and methods

Twenty-four parallelepiped beams,  $4 \times 4 \times 50\text{--}60$  mm, were sectioned from the cortex at the mid-diaphysis of a single bovine tibia. Two symmetric notches were machined on the periosteal surface of the beams, which were loaded in tension under bending, in order to concentrate damage ahead of the notch during loading. The notches were machined 10 mm

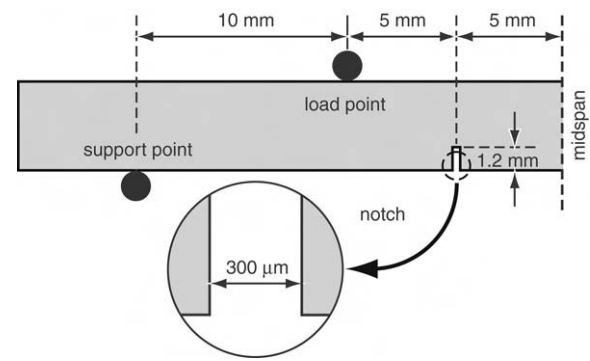


**Fig. 1 – Schematic diagram of a double-notched beam in four-point bending sectioned at the midspan, showing loading points and dimensions.**

apart to a depth of 1.2 mm and width of  $300\text{ }\mu\text{m}$  using a low-speed diamond wafer saw (Fig. 1). As-prepared beams were wrapped in gauze, hydrated with buffered saline solution, and stored at  $-20\text{ }^{\circ}\text{C}$  in airtight containers prior to mechanical testing and staining.

Specimens were randomly divided into six groups which were loaded in four-point bending fatigue to 0 (unloaded control),  $1 \times 10^5$ ,  $2 \times 10^5$ ,  $3 \times 10^5$ ,  $4 \times 10^5$  and  $5 \times 10^5$  cycles. A 5 N compressive preload was initially applied to each beam and the displacement was set to zero. Beams were loaded using an electromagnetic test instrument (ELF 3300, ElectroForce Systems Group of Bose Corp., Eden Prairie, MN) under displacement control (0.1 mm minimum and 0.3 mm maximum deflection) at a frequency of 2 Hz, while soaking in de-ionized water under ambient conditions. Loading was stopped after reaching the designated number of cycles or when fracture occurred at one of the notches, such that the unfractured notch exhibited the accumulation of microdamage prior to fracture (Nalla et al., 2003, 2005). Specimens that fractured prior to the designated number of cycles were reassigned to the appropriate group based on the number of cycles to failure. Load and displacement data were recorded continuously for 10 s for every 100 s. The beam stiffness ( $S$ , N/mm) was calculated as the secant from the maximum and minimum loads and displacements for each loading cycle recorded. The relative stiffness was calculated as the ratio of the stiffness at a given number of loading cycles to the initial stiffness and was correlated to the number of loading cycles using least-squares linear regression (JMP 5.1, SAS Institute, Inc., Cary, NC).

After mechanical loading, all beams were sectioned at the midspan (Fig. 1). For each beam, a specimen half with a notch that did not fracture was stained by  $\text{BaSO}_4$  precipitation, soaking in an equal parts mixture of 1 M barium chloride (certified ACS crystal, Fisher Scientific, Fair Lawn, NJ) in de-ionized water, buffered saline and acetone for 7 days, followed by an equal parts mixture of 1 M sodium sulfate (anhydrous powder, Fisher Scientific, Fair Lawn, NJ) in de-ionized water, buffered saline and acetone for 7 days, both under vacuum (50 mm Hg). Barium chloride and sodium sulfate staining solutions were neutralized by the addition of sodium hydroxide (ACS reagent, Sigma Chemical, St. Louis, MO) and nitric acid (ACS reagent, Aldrich Chemical,



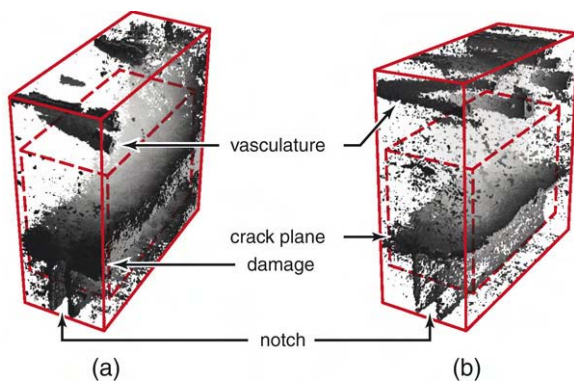


**Fig. 2 – Three-dimensional micro-CT images reconstructed from transverse slices of specimens loaded to  $5 \times 10^5$  cycles and stained with  $\text{BaSO}_4$ , showing (a) a typical specimen with a damaged region ahead of the notch and (b) a specimen with a macroscopic crack propagating laterally from the notch tip. The entire region imaged is shown by the solid box ( $1.6 \times 4.0 \times 4.0$  mm) and the subregion is shown by the dashed box ( $1.6 \times 2.0 \times 3.6$  mm). Note that  $\text{BaSO}_4$  also stained the endosteal vasculature shown at the top of each image and free surfaces of the beam, such as around the notch shown at the bottom of each image.**

Milwaukee, WI), respectively. The staining mechanism was a simple and benign precipitation reaction where  $\text{BaCl}_2(\text{aq}) + \text{Na}_2\text{SO}_4(\text{aq}) \rightarrow \text{BaSO}_4(\text{s}) + 2\text{NaCl}(\text{aq})$  (Leng et al., 2004).

Stained specimens were imaged using micro-CT ( $\mu\text{CT}$ -80, Scanco Medical AG, Bassersdorf, Switzerland) at 10  $\mu\text{m}$  resolution, 70 kVp voltage and 113  $\mu\text{A}$  current with slices taken either transversely or longitudinally. For transverse slices, a 1.6 mm long region of the entire specimen cross-section, which fully spanned the notch, was scanned using a 200 ms integration time. Longitudinal slices were imaged to a depth of 0.8 mm in the center of the specimen cross-section using a 300 ms integration time. In order to remove the effect of excess  $\text{BaSO}_4$  staining on the free surfaces of beams and within vasculature located near the endosteal surface, images reconstructed from transverse slices were also analyzed within a  $1.6 \times 2.0 \times 3.6$  mm subregion surrounding the notch tip. This subregion was located 1.4 mm from the endosteal surface, 0.6 mm from the periosteal surface and 0.2 mm from the beam sides (Fig. 2). Gaussian smoothing was applied to suppress noise and 3D images were thresholded in order to show the  $\text{BaSO}_4$  stain.

Damage was quantified from the micro-CT image intensity histogram which, after removing background pixels, represents the volume of material at a given image intensity. After staining with  $\text{BaSO}_4$ , the otherwise symmetric Gaussian distribution for bone was skewed to higher intensities due to the presence of  $\text{BaSO}_4$  (Fig. 3). Therefore, the single, asymmetric Gaussian peak in the image intensity histogram was fit as the sum of two symmetric Gaussian peaks, which represented the two known sources of x-ray attenuation (bone and  $\text{BaSO}_4$ ), using a non-linear least-squares algorithm (Fig. 3). The relative volume of stain was measured as the ratio of the  $\text{BaSO}_4$  integrated peak intensity relative to the total integrated peak intensity. Non-linear regression was used to

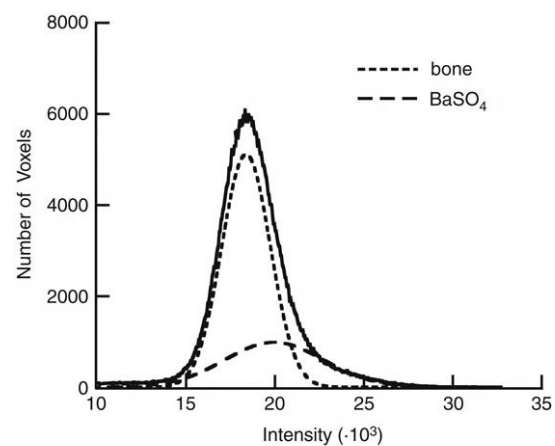


**Fig. 3 – Representative micro-CT image intensity histogram showing bone and  $\text{BaSO}_4$  peaks fit using a two-peaked Gaussian function.**

correlate the relative peak intensity for  $\text{BaSO}_4$  to the number of loading cycles using a power law (JMP 5.1, SAS Institute, Inc., Cary, NC). Regression analysis was conducted with all 24 specimens and after the exclusion of outlier specimens, which included two specimens that were over-stained and four specimens with macroscopic cracks present at the notch.

Selected specimens were also imaged by scanning electron microscopy (SEM) using backscattered electron imaging (BEI) (Evo 50, LEO Electron Microscopy Ltd., Cambridge, UK) at an accelerating voltage of 20 kV and a working distance of 7 mm. Note that image contrast in BEI is primarily due to compositional differences in atomic number, with increasing atomic number resulting in increased intensity. The elemental composition was also measured by electron probe microanalysis (EPMA) using energy dispersive spectroscopy (EDS) (INCA x-sight model 7636, Oxford Instruments America, Concord, MA). Specimens were embedded in poly(methylmethacrylate), sectioned with a low-speed diamond wafer saw, polished with a series of diamond compounds to a 0.25  $\mu\text{m}$  final finish, washed with methanol, dried overnight in an oven at 90 °C and coated with Au-Pd by sputter deposition.

Finite element analysis (FEA) was used to qualitatively compare principal strain contours around the notch to micro-CT images of the staining. The finite element model was created with four-node plane strain elements and analyzed with ABAQUS (v.6.3, ABAQUS, Inc., Providence, RI). Isotropic material properties were assigned to the bone tissue, using an elastic modulus of 18 GPa (Reilly and Burstein, 1974) and Poisson's ratio of 0.3. Displacement bounding conditions were applied to simulate the maximum deflection in four-point bending.

### 3. Results

Micro-CT images of damaged specimens showed high-intensity voxels within the bone tissue in regions ahead of the notch tip, as well as on surfaces associated with specimen

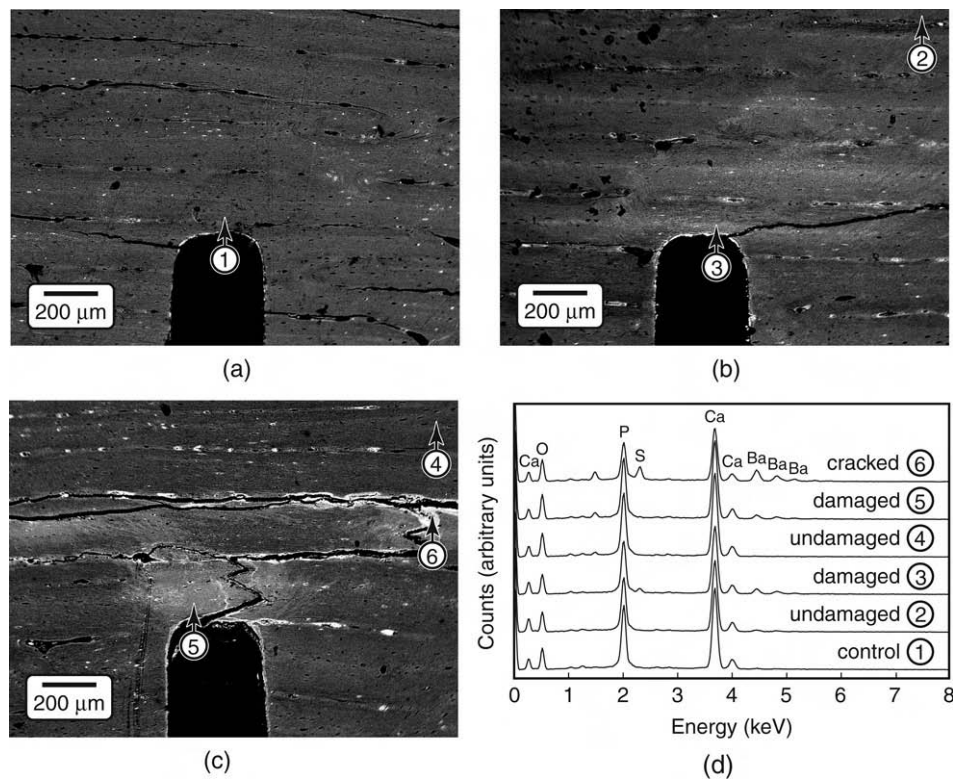


**Fig. 4** – SEM micrographs using BEI showing (a) an unloaded control specimen and specimens loaded to  $5 \times 10^5$  cycles exhibiting (b) microdamage accumulation ahead of the notch and (c) a crack that propagated from the notch. All specimens were stained with  $\text{BaSO}_4$ . (d) The elemental composition was measured using EDS at the locations shown in undamaged tissue, damaged tissue and the within the crack. Note that the specimen shown in Fig. 4(a) is the same as that shown in Fig. 6 (unloaded control); the specimen shown in Fig. 4(b) is the same as that shown in Fig. 2(a) and Fig. 6 ( $5 \times 10^5$  cycles); and the specimen shown in Fig. 4(c) is the same as that shown in Figs. 2(b) and 9.

edges, propagating cracks and vasculature (Fig. 2). These high-intensity voxels were observed at higher resolution and shown to be due to the presence of precipitated  $\text{BaSO}_4$  using BEI and EDS, respectively (Fig. 4). The highest image intensity and highest levels of elemental barium (Ba) and sulfur (S) were detected within propagating cracks (Fig. 4, location 6) or vasculature (Fig. 2). Lower levels of Ba and S were detected in damaged tissue ahead of the notch, which appeared at an intermediate image intensity (Fig. 4, locations 3 and 5). The stain was virtually undetectable within the unloaded control specimen or regions of tissue far away from the notch, where the lowest image intensity was observed and no damage was expected (Fig. 4, locations 1, 2 and 4). Note that the absence of  $\text{BaSO}_4$  within cracks allowed drying cracks (e.g., Fig. 4(a), (b)) to be distinguished from cracks that initiated and propagated during loading (e.g., Fig. 4(c)). Higher-magnification SEM micrographs revealed the presence of individual  $\text{BaSO}_4$  crystals, less than  $5 \mu\text{m}$  in size, on the surfaces of propagating cracks (Fig. 5(a)) and diffuse staining within damaged tissue (Fig. 5(b)). Thus,  $\text{BaSO}_4$  staining enhanced the contrast of tissue that was damaged during loading which enabled imaging by micro-CT using a suitable threshold intensity.

The amount of staining ahead of the notch tip visibly increased with an increased number of loading cycles, as shown by representative two-dimensional micro-CT images

from different specimens (Fig. 6). Note that unloaded control specimens exhibited negligible staining ahead of the notch but did exhibit staining of vasculature and the free surfaces of beams (Fig. 4(a) and Fig. 6). Furthermore, the shape of stained regions ahead of the notch tip was qualitatively consistent with principal strain contours calculated by FEA, which exhibited a characteristic kidney shape of high intensity immediately ahead of the notch (Fig. 7).

The amount of staining was measured from micro-CT image histograms by the ratio of the  $\text{BaSO}_4$  integrated peak intensity relative to the overall integrated peak intensity (Fig. 3), and was correlated with the number of loading cycles using a power-law regression (Fig. 8, Table 1). The strength and significance of the correlation was improved using a subregion that excluded the free surfaces of beams and endosteal vasculature (Fig. 2, Table 1). The correlation was also improved by excluding two specimens that were observed to be over-stained and four specimens that exhibited macroscopic cracks propagating from the imaged notch, rather than only microdamage ahead of the notch (Fig. 8, Table 1).

#### 4. Discussion

The accumulation of microdamage during fatigue was non-destructively and three-dimensionally imaged in notched

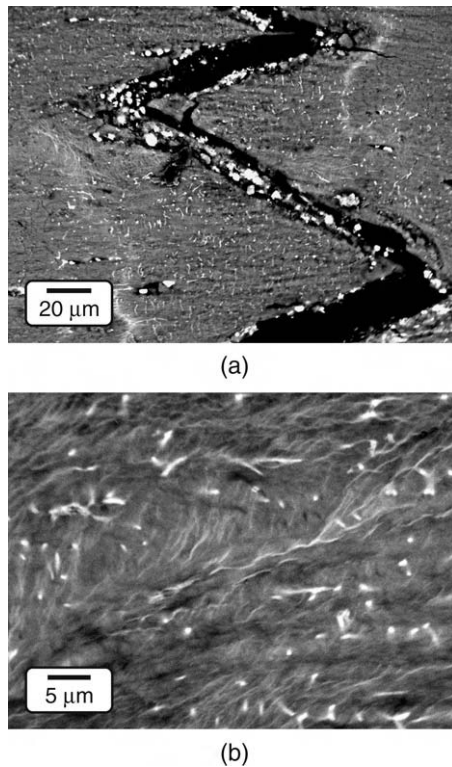


**Fig. 5 – Higher-magnification SEM micrographs using BEI for specimens loaded to  $5 \times 10^5$  cycles showing (a) a crack that propagated from the notch (Fig. 4(c)) and (b) diffuse staining of damage ahead of the notch (Fig. 4(b), location 3). Note the presence of  $\text{BaSO}_4$  crystals within the crack, staining of canaliculi, and characteristic wavy lines for diffuse damage.**

bovine cortical bone beams *in vitro* using micro-CT with a new  $\text{BaSO}_4$  staining technique (Figs. 2 and 6).  $\text{BaSO}_4$  was precipitated within damaged tissue, cracks and vasculature, and enhanced the intensity of voxels in micro-CT due to the higher x-ray attenuation of  $\text{BaSO}_4$  relative to bone tissue (Figs. 2 and 4). The amount of staining was measured from the image intensity histogram and correlated with the number of loading cycles using a power-law regression (Fig. 8). Thus, this

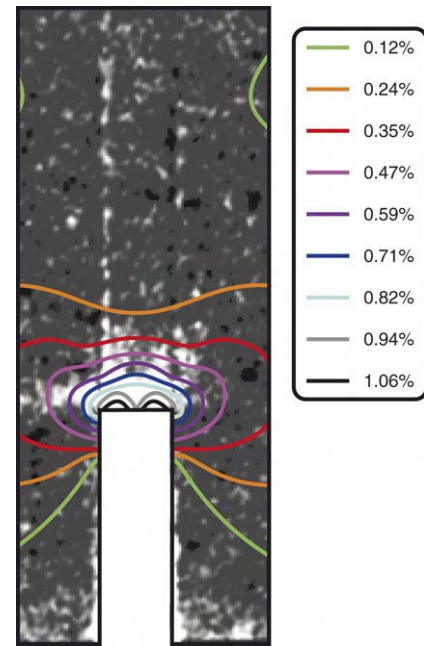


**Fig. 7 – Two-dimensional micro-CT image of a specimen loaded to  $1 \times 10^5$  cycles showing the shape of the stained region ahead of the notch in comparison to principal strain contours calculated by FEA.**

study demonstrated the feasibility of non-destructive and three-dimensional detection of microdamage in cortical bone *in vitro* using micro-CT with a suitable contrast agent.

Staining occurred via a simple and benign precipitation reaction (Leng et al., 2004). Specimens were soaked in supersaturated staining solutions such that barium and sulfate ions diffused and concentrated within void space in the tissue – e.g., vasculature and cracks – which acted as a “micro-reactor” and provided an abundance of heterogeneous nucleation sites on surfaces of the extracellular matrix. The presence of  $\text{BaSO}_4$  was verified by BEI and EDS (Fig. 4). Furthermore, individual crystals less than  $5 \mu\text{m}$  in size were observed on the surfaces of propagating cracks at high magnification (Fig. 5(a)). These crystals appeared similar to those prepared under more

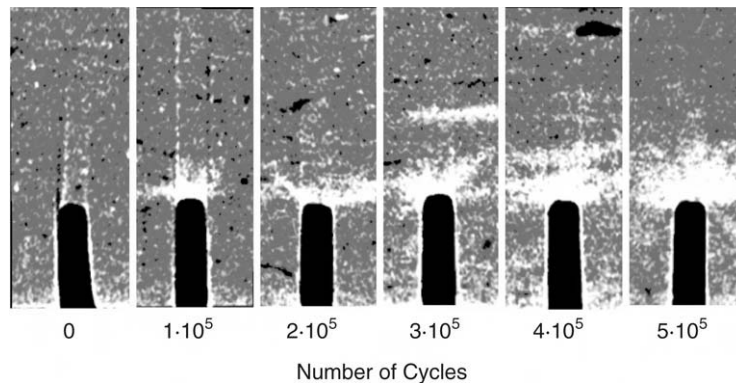


**Fig. 6 – Representative two-dimensional micro-CT images from different specimens showing changes in the stained region ahead of the notch with the number of loading cycles. The images were taken from specimens loaded to 0 (control),  $1 \times 10^5$ ,  $2 \times 10^5$ ,  $3 \times 10^5$ ,  $4 \times 10^5$  and  $5 \times 10^5$  cycles (left to right). The width of each image is 1.2 mm.**



**Table 1 – Non-linear regression of the BaSO<sub>4</sub> relative peak intensity with the number of loading cycles using a power law,  $y = A \cdot x^b$ . The region of analysis included either the micro-CT image of the entire specimen cross-section or a subregion that excluded the free surfaces of beams and endosteal vasculature, as shown in Fig. 2. Specimens regarded as outliers included two specimens that were observed to be over-stained and four specimens that exhibited macroscopic cracks propagating from the imaged notch (Fig. 8)**

| Specimens                 | Region of analysis   | A     | b     | p       | r <sup>2</sup> |
|---------------------------|----------------------|-------|-------|---------|----------------|
| All (n = 24)              | Entire cross-section | 0.165 | 0.041 | <0.05   | 0.23           |
| All (n = 24)              | Subregion            | 0.063 | 0.121 | <0.0001 | 0.56           |
| Outliers removed (n = 18) | Entire cross-section | 0.162 | 0.045 | <0.005  | 0.41           |
| Outliers removed (n = 18) | Subregion            | 0.062 | 0.124 | <0.0001 | 0.61           |

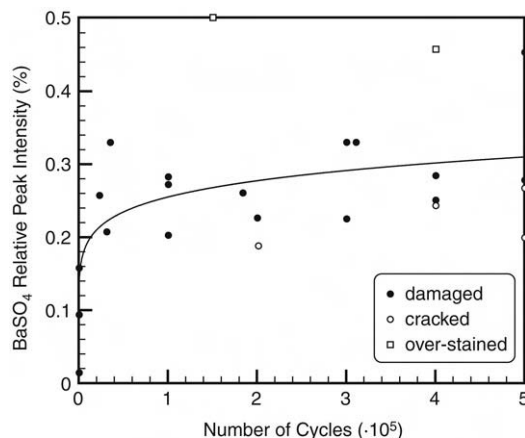


**Fig. 8 – Power-law regression of the BaSO<sub>4</sub> relative peak intensity with the number of loading cycles using the image subregion and including all specimens,  $y = 0.063x^{0.121}$  ( $p < 0.0001$ ,  $r^2 = 0.56$ ). Data points considered as outliers in subsequent regression analyses, shown in Table 1, included two specimens that were observed to be over-stained and four specimens that exhibited macroscopic cracks propagating from the imaged notch.**

highly controlled conditions (Leng et al., 2004). Staining was not observed in tissue ahead of the notch in unloaded control specimens or far away from the notch in loaded specimens (Fig. 4). Therefore, the observed staining of tissue ahead of the notch tip in loaded specimens suggests that damage resulted in the extra-cellular matrix having an increased permeability to the staining solutions due to ultrastructural (“diffuse”) damage. Higher-magnification SEM micrographs revealed “diffuse staining” and “diffuse damage” (Fig. 5(b)) similar to observations with BEI using a lead-uranyl acetate stain (Schaffler et al., 1994) and ultraviolet light or confocal microscopy using fluorescent stains or chelating agents (Boyce et al., 1998; Martin, 2003; Wang and Niebur, 2006; Zioupos and Currey, 1994).

The region of diffuse staining ahead of the notch tip did not extend as far ahead of the notch in specimens where a macroscopic crack propagated from the notch (Fig. 2(b), Fig. 4(c) and Fig. 8). In such cases, the crack propagated laterally from the notch, due to the orientation of the notch relative to the plexiform (or fibrolamellar) structure of bovine cortical bone, and the crack plane was able to be imaged using longitudinal slices in micro-CT (Fig. 9). The smaller

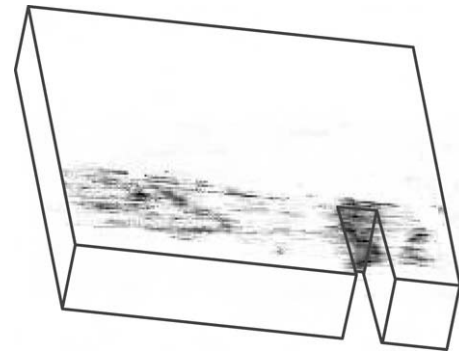


**Fig. 9 – Three-dimensional micro-CT image reconstructed from longitudinal slices of a specimen loaded to  $5 \times 10^5$  cycles and stained with BaSO<sub>4</sub>, showing a crack propagating laterally from the notch. Note that the specimen is the same as that shown in Fig. 2(b) and Fig. 4(c).**

region of diffuse staining ahead of the notch in cracked specimens suggests that damage accumulation occurred primarily before, rather than during, crack propagation. Similarly, studies investigating the toughness of cortical bone during crack propagation (R-curve behavior) have concluded that microcracking contributes relatively little as a toughening mechanism, per se (Ager et al., 2006; Nalla et al., 2004, 2005). Thus, the role of microcracking is more likely as a precursor to crack propagation (Ager et al., 2006; O'Brien et al., 2005) rather than a toughening mechanism during crack propagation (Vashishth et al., 1997, 2000).

The amount of BaSO<sub>4</sub> staining was correlated with the number of loading cycles using a power-law regression (Fig. 8, Table 1). The power-law relationship was not surprising since specimens were loaded under displacement control, where damage accumulation was expected to lower the beam stiffness and thus the applied load with increasing loading cycles. Since BaSO<sub>4</sub> staining was shown to be due to microdamage, the amount of BaSO<sub>4</sub> staining was considered a relative, but not an absolute, measure of damage. This was a limitation of the study design where only one unbroken notch from each specimen was consistently suitable for imaging microdamage and was stained only with BaSO<sub>4</sub>. If loaded specimens were sectioned lengthwise prior to staining, matching pairs could be stained and imaged by both micro-CT using BaSO<sub>4</sub> and ultraviolet light microscopy using a fluorescent stain or chelating agent. Thus, a direct correlation could be made between each measure of damage, and such a study is in progress.

The strength and significance of the correlation for the amount of BaSO<sub>4</sub> staining with the number of loading cycles was substantially improved using a subregion that excluded non-specific staining of the free surfaces of beams and endosteal vasculature (Table 1). In particular, the presence and amount of endosteal vasculature was randomly distributed amongst specimens, but had a profound influence on the staining volume when present (cf. Fig. 2(a) vs. (b)). The correlation was also improved by excluding six specimens exhibiting atypical behavior that was ascribed to the study methods. On average, the four specimens with macroscopic cracks propagating laterally from the unbroken notch exhibited less diffuse staining ahead of the notch (Figs. 2 and 8), for reasons discussed above. On the other hand, the reason for the apparent over-staining of two specimens was not clear. These specimens exhibited homogeneous staining of up to one-half the specimen cross-section that was clearly unrelated to the notch, loading or tissue microstructure.

Each loaded beam exhibited a continuous decrease in stiffness with the number of loading cycles, as expected. The amount of staining was correlated with the total (%) stiffness loss using a power-law regression ( $p < 0.05$  for all sets of data shown in Table 1). However, the total (%) loss in stiffness was not correlated with the number of loading cycles ( $p = 0.51$  and  $0.26$  for  $n = 24$  and  $18$ , respectively). There are a couple of plausible explanations for this unexpected behavior. Specimens with macroscopic cracks propagating laterally from the unbroken notch exhibited less diffuse staining ahead of the notch, as described above, but a greater and more rapid stiffness loss. This explanation logically leads to a question of why the unbroken notch in most specimens exhibited damage accumulation ahead of the notch, but several specimens exhibited cracks propagating from the notch. The use of double-notched beams is a clever experimental technique that was previously used to characterize conditions ahead of the unbroken notch after static loading with the assumption that conditions ahead of the unbroken notch are reflective of the broken notch just prior to failure (Nalla et al., 2003, 2005). In this study, double-notched beams were loaded in displacement controlled fatigue and the same assumption was made. Thus, the results of this study may call this assumption into question, perhaps due to the heterogeneity of bone tissue ahead of each notch.

In summary, BaSO<sub>4</sub> staining enabled non-destructive and three-dimensional detection of microdamage in cortical bone using micro-CT. The amount of staining was qualitatively and quantitatively correlated with microdamage accumulation. Therefore, the methods in this study may be useful for future *in vitro* studies into the role of microdamage in bone fragility by enabling correlation of the spatial density of microdamage accumulation to local variations in mechanical loading, bone mineral density (BMD) or microarchitecture. Extension of this technique to *in vivo* detection of microdamage will require improved specificity, biocompatibility, deliverability and x-ray dosage. Staining by BaSO<sub>4</sub> precipitation was non-specific for damage, including all void spaces such as vasculature and free surfaces, and the staining solutions were not biocompatible. Specificity could be greatly improved by molecular or particulate contrast agents with functional

groups that enable preferential binding to calcium exposed on the surfaces of microcracks or diffuse damage (Parkesh et al., 2007). Such a contrast agent could be delivered during the accumulation of damage in bone *in situ*. Finally, the x-ray dosage of current micro-CT scanners is not yet suitable for imaging *in vivo*, though it is not known whether a suitable contrast agent could enable the detection of damaged tissue using clinical CT scanners.

## 5. Conclusions

Non-destructive and three-dimensional detection of fatigue microdamage accumulation in notched cortical bone specimens was enabled *in vitro* using micro-CT with a precipitated BaSO<sub>4</sub> contrast agent. Reconstructed images showed a distinct region of bright voxels around the notch tip or along propagating cracks due to the presence of BaSO<sub>4</sub>, which was verified by backscattered electron imaging and energy dispersive spectroscopy. The shape of the stained region ahead of the notch tip was qualitatively consistent with principal strain contours calculated by finite element analysis. The relative volume of the stained region was correlated with the number of loading cycles by non-linear regression using a power law. The new methods demonstrated in this study may be useful for future *in vitro* studies into the role of microdamage in bone fragility.

## Acknowledgements

This research was supported by the National Institutes of Health (AR049598) and U.S. Army Medical Research and Materiel Command (W81XWH-06-1-0196) through the Department of Defense Peer Reviewed Medical Research Program (PR054672).

## REFERENCES

- Ager III, J.W., Balooch, G., Ritchie, R.O., 2006. Fracture, aging, and disease in bone. *J. Mater. Res.* 21 (8), 1878–1892.
- Boyce, T.M., Fyhrie, D.F., Glotkowski, M.C., Radin, E.L., Schaffler, M.B., 1998. Damage type and strain mode associations in human compact bone bending fatigue. *J. Orthop. Res.* 16 (5), 322–329.
- Burr, D.B., Martin, R.B., Schaffler, M.B., Radin, E.L., 1985. Bone remodeling in response to *in vivo* fatigue microdamage. *J. Biomech.* 18, 189–200.
- Burr, D.B., Stafford, T., 1990. Validity of the bulk-staining technique to separate artefactual from *in vivo* bone microdamage. *Clin. Orthop. Rel. Res.* (260), 305–308.
- Burr, D.B., Forwood, M.R., Fyhrie, D.P., Martin, R.B., Schaffler, M.B., Turner, C.H., 1997. Bone microdamage and skeletal fragility in osteoporotic and stress fractures. *J. Bone Miner. Res.* 12, 6–15.
- Jee, W.S.S., 2001. Integrated bone tissue physiology: anatomy and physiology. In: Cowin, S.C. (Ed.), *Bone Mechanics Handbook*, second ed. CRC Press LLC, Boca Raton, pp. 1.1–1.68.
- Jepsen, K.J., Davy, D.T., 1997. Comparison of damage accumulation measures in human cortical bone. *J. Biomech.* 30 (9), 891–894.
- Lee, T.C., Arthur, T.L., Gibson, L.J., Hayes, W.C., 2000. Sequential labelling of microdamage in bone using chelating agents. *J. Orthop. Res.* 18, 322–325.

- Leng, H., Wang, X., Niebur, G.L., Roeder, R.K., 2004. Synthesis of a barium sulfate nanoparticle contrast agent for micro-computed tomography of bone microstructure. *Ceram. Trans.* 159, 219–229.
- Leng, H., VanDersarl, J.J., Niebur, G.L., Roeder, R.K., 2005. Microdamage in bovine cortical bone measured using micro-computed tomography. *Trans. Orthop. Res. Soc.* 30, 665.
- Lewis, G., 1997. Properties of acrylic bone cement: State of the art review. *J. Biomed. Mater. Res. (Appl. Biomater.)* 38, 155–182.
- Li, J., Miller, M.A., Hutchins, G.D., Burr, D.B., 2005. Imaging bone microdamage in vivo with positron emission tomography. *Bone* 37 (6), 819–824.
- Martin, R.B., Burr, D.B., 1982. A hypothetical mechanism for the stimulation of osteonal remodelling by fatigue damage. *J. Biomech.* 15 (3), 137–139.
- Martin, R.B., 2003. Fatigue microdamage as an essential element of bone mechanics and biology. *Calcif. Tissue Int.* 73 (2), 101–107.
- Mori, S., Burr, D.B., 1993. Increased intracortical remodeling following fatigue damage. *Bone* 14, 103–109.
- Nalla, R.K., Kinney, J.H., Ritchie, R.O., 2003. Mechanistic fracture criteria for the failure of human cortical bone. *Nat. Mater.* 2, 164–168.
- Nalla, R.K., Kruzic, J.J., Ritchie, R.O., 2004. On the origin of the toughness of mineralized tissue: microcracking or crack bridging? *Bone* 34, 790–798.
- Nalla, R.K., Stölken, J.S., Kinney, J.H., Ritchie, R.O., 2005. Fracture in human cortical bone: local fracture criteria and toughening mechanisms. *J. Biomech.* 38, 1517–1525.
- O'Brien, F.J., Taylor, D., Dickson, G.R., Lee, T.C., 2000. Visualization of three-dimensional microcracks in compact bone. *J. Anat.* 197, 413–420.
- O'Brien, F.J., Taylor, D., Lee, T.C., 2002. An improved labelling technique for monitoring microcrack growth in compact bone. *J. Biomech.* 35, 523–526.
- O'Brien, F.J., Taylor, D., Lee, T.C., 2005. The effect of bone microstructure on the initiation and growth of microcracks. *J. Orthop. Res.* 23 (2), 475–480.
- Parkesh, R., Lee, T.C., Gunnlaugsson, T., Gowin, W., 2006. Microdamage in bone: Surface analysis and radiological detection. *J. Biomech.* 39, 1552–1556.
- Parkesh, R., Mohsin, S., Lee, T.C., Gunnlaugsson, T., 2007. Histological, spectroscopic, and surface analysis of microdamage in bone: Toward real-time analysis using fluorescent sensors. *Chem. Mater.* 19, 1656–1663.
- Reilly, D.T., Burstein, A.H., 1974. The mechanical properties of cortical bone. *J. Bone Joint Surg. Am.* 56 (5), 1001–1022.
- Schaffler, M.B., Radin, E.L., Burr, D.B., 1989. Mechanical and morphological effects of strain rate on fatigue of compact bone. *Bone* 10 (3), 207–214.
- Schaffler, M.B., Pitchford, W., Choi, K., Riddle, J.M., 1994. Examination of compact bone microdamage using back-scattered electron microscopy. *Bone* 15, 483–488.
- Silva, M.J., Uthgenannt, B.A., Rutlin, J.R., Wohl, G.R., Lewis, J.S., Welch, M.J., 2006. In vivo skeletal imaging of <sup>18</sup>F-fluoride with positron emission tomography reveals damage- and time-dependent responses to fatigue loading in the rat ulna. *Bone* 39, 229–236.
- Skucas, J., 1989. Barium sulfate: Clinical Application, Barium sulfate: Toxicity and Complications. In: Skucas, J. (Ed.), *Radiographic Contrast Agents*, second ed. Aspen Publishers, Inc., Rockville, pp. 10–76.
- Vashishth, D., Behiri, J.C., Bonfield, W., 1997. Crack growth resistance in cortical bone: Concept of microcrack toughening. *J. Biomech.* 30, 763–769.
- Vashishth, D., Tanner, K.E., Bonfield, W., 2000. Contribution, development and morphology of microcracking in cortical bone during crack propagation. *J. Biomech.* 33, 1169–1174.
- Wang, X., Niebur, G.L., 2006. Microdamage propagation in trabecular bone due to changes in loading mode. *J. Biomech.* 39, 781–790.
- Wang, X., Masse, D.B., Leng, H., Hess, K.P., Ross, R.D., Roeder, R.K., Niebur, G.L., 2007. Detection of trabecular bone microdamage by micro-computed tomography. *J. Biomech.*, in press (doi:10.1016/j.jbiomech.2007.05.009).
- Zioupou, P., Currey, J.D., 1994. The extent of microcracking and the morphology of microcracks in damaged bone. *J. Mater. Sci.* 29, 978–986.



# Detection of trabecular bone microdamage by micro-computed tomography

Xiang Wang, Daniel B. Masse, Huijie Leng, Kevin P. Hess, Ryan D. Ross,  
Ryan K. Roeder, Glen L. Niebur\*

*Tissue Mechanics Laboratory, Department of Aerospace and Mechanical Engineering, University of Notre Dame, Notre Dame, IN 46556, USA*

Accepted 10 May 2007

---

## Abstract

Microdamage is an important component of bone quality and affects bone remodeling. Improved techniques to assess microdamage without the need for histological sectioning would provide insight into the role of microdamage in trabecular bone strength by allowing the spatial distribution of damage within the trabecular microstructure to be measured. Nineteen cylindrical trabecular bone specimens were prepared and assigned to two groups. The specimens in group I were damaged to 3% compressive strain and labeled with BaSO<sub>4</sub>. Group II was not loaded, but was labeled with BaSO<sub>4</sub>. Micro-computed tomography (Micro-CT) images of the specimens were obtained at 10 μm resolution. The median intensity of the treated bone tissue was compared between groups. Thresholding was also used to measure the damaged area fraction in the micro-CT scans. The histologically measured damaged area fraction, the median CT intensity, and the micro-CT measured damaged area fraction were all higher in the loaded group than in the unloaded group, indicating that the micro-CT images could differentiate the damaged specimen group from the unloaded specimens. The histologically measured damaged area fraction was positively correlated with the micro-CT measured damaged area fraction and with the median CT intensity of the bone, indicating that the micro-CT images can detect microdamage in trabecular bone with sufficient accuracy to differentiate damage levels between samples. This technique provides a means to non-invasively assess the three-dimensional distribution of microdamage within trabecular bone test specimens and could be used to gain insight into the role of trabecular architecture in microdamage formation.

© 2007 Elsevier Ltd. All rights reserved.

**Keywords:** Microdamage; Cancellous bone; Computed tomography; Contrast agents; Bone mechanics

---

## 1. Introduction

Microdamage is one factor commonly associated with bone quality. The presence of microdamage decreases the apparent level mechanical properties of trabecular bone (Wachtel and Keaveny, 1997) and can propagate under loading (Wang and Niebur, 2006; Wang et al., 2005), which may increase fracture risk. Microdamage also stimulates adaptive remodeling (Burr, et al., 1985). As such, experimental studies of microdamage formation (Arthur Moore and Gibson, 2002) and propagation (Wang and Niebur, 2006; Wang et al., 2005) should improve our understanding of both bone fragility and mechanobiology. Techniques to assess microdamage that allow further mechanical testing

could enhance capabilities to study microdamage effects on bone fragility. Spatial quantification of microdamage in three dimensions would also provide a means to quantify the localization of microdamage with respect to trabecular architecture and loading conditions, which could in turn provide further insight into the relative roles of microdamage and architecture in trabecular bone strength and adaptation.

Measurements of microdamage in bone, first reported by Frost in 1960 (Frost, 1960), have a long history. Bulk labeling followed by microscopic imaging of thin sections is the gold standard for quantifying damage (Burr and Stafford, 1990). However, it provides only a two-dimensional representation of the distribution and density of damage. Three-dimensional images of single microcracks in trabecular (Fazzalari et al., 1998) and cortical bone (O'Brien et al., 2000), obtained by reconstructing serial

---

\*Corresponding author. Tel.: +1 574 631 3327; fax: +1 574 631 2144.  
E-mail address: [gniebur@nd.edu](mailto:gniebur@nd.edu) (G.L. Niebur).

sections of two-dimensional confocal microscopy images, demonstrated that cracks were elliptical in shape (O'Brien et al., 2000). This technique is powerful for evaluating individual cracks or damaged regions, but can provide only limited information on the spatial distribution of microdamage, because the observation depth is limited to about 160  $\mu\text{m}$  from the surface (Fazzalari et al., 1998; O'Brien et al., 2000) and the field of view is small. Microdamage due to non-uniform loading modes, such as torsion, has been studied by accounting for changes in the strain level (Wang and Niebur, 2006; Wang et al., 2005), but was again limited to a few two-dimensional sections for each test specimen. The use of thin sections also resulted in loss of information regarding the surrounding trabecular structure, limiting the ability to assess the effects of architecture on microdamage formation. Recently, an iodine-based, calcium-chelating contrast agent was used to image a scratch on the surface of a bone sample using micro-computed tomography (micro-CT) (Lee et al., 2003; Parkesh et al., 2006). Synchrotron radiation sources can provide very high-resolution images that allow direct visualization of microcracks (Thurner et al., 2006). However, availability of such imaging systems is limited.

The ability to detect microdamage using radiological imaging would provide a powerful set of tools to improve our understanding of the role of microdamage in bone fragility. Although microcracks are too small to be visualized using commercial micro-CT systems, contrast agents may allow a three-dimensional assessment of microdamage density and spatial distribution. The goal of this study was to validate a technique for detecting the presence of microdamage in trabecular bone using micro-CT imaging. Specifically, the aims were to: (1) develop a protocol for labeling microdamage in trabecular bone with barium sulfate ( $\text{BaSO}_4$ ); (2) apply the technique to detect microdamage induced in bovine tibial trabecular bone specimens, and (3) correlate the micro-CT imaging results with histological measurements of microdamage.

## 2. Methods

Thirty cylindrical trabecular bone specimens were prepared from eight bovine tibiae. The specimens were cored along the anatomical axis of the tibia using a diamond coring drill (Starlite Industries, Bryn Mawr, PA) (Wang et al., 2004). The diameter of the specimens was  $8.21 \pm 0.04$  mm (mean  $\pm$  std. dev.). The prepared specimens were wrapped in gauze saturated with buffered saline solution and stored at  $-20^\circ\text{C}$  in airtight containers except during mechanical testing and labeling. Specimens were assigned to one of two groups. In group I, ten specimens were damaged by a compressive overload and subsequently treated by  $\text{BaSO}_4$  precipitation. Group II (11 specimens) was not loaded, but was treated by  $\text{BaSO}_4$  precipitation, and group III (nine specimens) was neither loaded nor treated.

The specimens in group I were first glued into brass endcaps (Keaveny et al., 1997), which were subsequently clamped into a servo-hydraulic load frame (model 8821s, Instron Corp. Canton, MA) for testing. Strains were measured by an extensometer (model 3550, Epsilon Technology Corp., Jackson, WY) attached to the endcaps. The effective gage length was taken as the exposed plus half the embedded length of the specimen (Keaveny et al., 1997). All tests were performed at room temperature, and

the exposed portion of the specimen was wrapped in gauze saturated with buffered saline solution for hydration.

The undamaged Young's modulus of each specimen was first measured non-destructively. The specimens were loaded in compression three times from 0% to 0.4% strain at a rate of 0.5% per second, and the apparent Young's modulus was calculated from a second order polynomial fit to the stress strain data over a strain range from 0–0.2% (Morgan et al., 2001). Next, damage was induced by overloading the specimens in compression to 3% strain at 0.5% strain per second, which has been shown to induce microdamage in trabecular bone (Arthur Moore and Gibson, 2002; Keaveny et al., 1994; Wang and Niebur, 2006). The damaged Young's modulus was subsequently measured with three additional non-destructive loading cycles. Afterward, the specimens were sectioned from endcaps using a low speed diamond saw (Isomet, Buehler Ltd., Lake Bluff, IL).

The specimens in groups I and II were treated by precipitation of  $\text{BaSO}_4$ . Marrow was removed using a water jet while specimens were submerged in water to avoid additional damage. They were then treated by soaking in an aqueous solution of 0.5 M  $\text{BaCl}_2$  (Certified ACS crystal, Fisher Scientific, Fair Lawn, NJ) for 48 h under vacuum, followed by 48 h in an aqueous solution of 0.5 M  $\text{NaSO}_4$  (Anhydrous powder, Fisher Scientific, Fair Lawn, NJ) under vacuum. Finally, the specimens were agitated in buffered saline solution to remove excess  $\text{BaSO}_4$  precipitates for 1 h.

All specimens were imaged by micro-CT ( $\mu\text{CT}$ -80, Scanco Medical AG, Bassersdorf, Switzerland) at 10  $\mu\text{m}$  in-plane resolution and 10  $\mu\text{m}$  slice thickness. The X-ray source voltage was 45 kVp, the source current was 177  $\mu\text{A}$ , and the integration time was 400 ms per projection. Image slices were taken along the axis of the specimen, in order to capture any localized regions of damage along the length (Arthur Moore and Gibson, 2002). Ten images were captured at the specimen axis, as well as at 1 and 2.5 mm above and below the specimen axis (Fig. 1). In total, approximately 8% of the specimen volume was imaged. This protocol provided image data for a representative volume of each specimen while limiting scanning time. A  $5 \times 5$  mm<sup>2</sup> region ( $500 \times 500$  pixels) from each scan was selected for analysis to avoid the edges of the specimen, where damage might be induced during sectioning or specimen preparation. One specimen in group I was eliminated, because the sectioned length of the sample was less than 5 mm. The raw images were filtered by a Gaussian filter with  $\sigma = 1$  and support 2 (Scanco, 1999).

Intensity histograms were obtained from the selected regions of each reconstructed micro-CT. The intensity histograms were fit using a double peaked Gaussian function:

$$N(I) = a_1 e^{-(I-\mu_1)^2/2\sigma_1^2} + a_2 e^{-(I-\mu_2)^2/2\sigma_2^2}, \quad (1)$$

where  $I$  is the micro-CT intensity,  $N$  is the number of voxels with intensity  $I$ ,  $\mu_1$  and  $\mu_2$  are the median intensities of each peak,  $\sigma_1$  and  $\sigma_2$  control the peak width, and  $a_1$  and  $a_2$  scale the height of the peaks. The first peak represented the marrow space, while the second represented the bone tissue. The median intensity was used as a measure of  $\text{BaSO}_4$  uptake in the specimens. The volume fraction of each sample was estimated by dividing the number of voxels with values in the range  $\mu_2 \pm 3.5\sigma_2$  by the total number of image voxels.

Thresholding was used to determine the fraction of damaged bone tissue in each specimen. Voxels with intensities greater than 9000 (corresponding to a linear attenuation of  $2.20 \text{ mm}^{-1}$ ) were taken to be bone tissue, and those with intensities greater than 23,500 (corresponding to a linear attenuation of  $5.74 \text{ mm}^{-1}$ ) were taken to be  $\text{BaSO}_4$  labeled damage. These thresholds were determined by parametrically varying the values and visualizing the resulting images (Fig. 2). The lower threshold was appropriate for detecting the bone tissue in untreated specimens as well as treated specimens, while no voxels exceeded the upper threshold in untreated specimens. The  $\text{BaSO}_4$  labeled damage fraction ( $\text{Dx.Ar}_{\text{CT}}$ ) was defined as the number of labeled voxels divided by the number of bone voxels.

Thin sections were prepared for histologic quantification of microdamage of the specimens in both experimental groups. No staining (e.g. basic fuchsin) was used for the histology sections, as they may have interfered with the  $\text{BaSO}_4$  labeling. The specimens were gradually

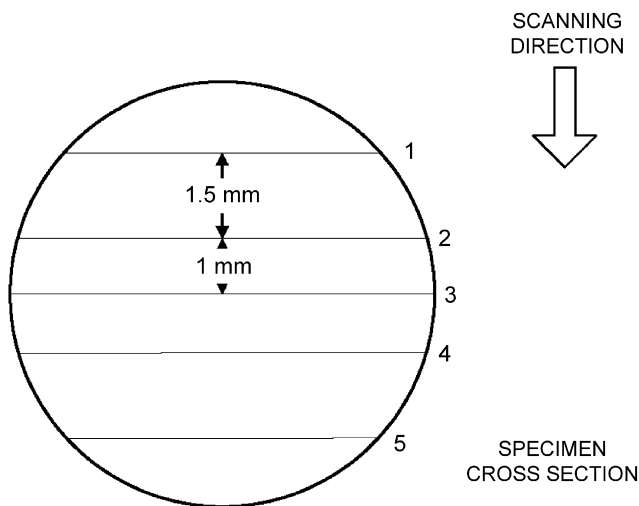


Fig. 1. At every scanning position (1–5), groups of ten images spaced 10  $\mu\text{m}$  apart were obtained. One group was located at the specimen axis, two were centered 1 mm above and below the axis, and two were centered 2.5 mm above and below the axis.

dehydrated in a series of ethanol solutions (Lee et al., 1998; O'Brien et al., 2000), then embedded in transparent polymethyl methacrylate (Aldrich Chemical Company, Inc., Milwaukee, WI) under vacuum. One 200  $\mu\text{m}$  thick section was cut along the axis of each specimen using a diamond wafer saw. The surfaces of the sections were polished with a series of abrasives beginning with 600 grit paper and ending with 1/4  $\mu\text{m}$  diamond paste (Phoenix Beta, Buehler, Lake Bluff, IL). The final thickness of the polished sections was approximately 150  $\mu\text{m}$ . Polished sections were mounted on glass slides using Eukitt's mounting medium (American Histology Reagent Company, Inc., Hawthorne, NY) and glass cover slips. One sample from group I was eliminated because the histologic section was destroyed during processing.

The slices were imaged with reflected light microscopy (Eclipse ME 600, Nikon Inc., Melville, NY). Images of 20 randomly selected regions were captured from each section at 200 $\times$  magnification. Each image had an area of 0.39 mm<sup>2</sup>. Microdamage was quantified in each section by area counting. A 25  $\times$  20 grid with 28  $\mu\text{m}$  edge squares was superimposed on each image (Fig. 3). The number of squares containing microcracks was counted in each section. The ratio of the number of squares containing microcracks to those containing bone was defined as the damaged area fraction (Dx.Ar.H). Because the histological measurement of damaged area fraction may be sensitive to the selected grid size, the analysis was repeated using a grid with 56  $\mu\text{m}$  spacing.

In order to verify that BaSO<sub>4</sub> was present in damaged regions, two specimens from each treated group were imaged by back-scattered scanning electron microscopy (SEM) (Evo 50, LEO Electron Microscopy Ltd., Cambridge, UK). Back-scattered SEM provides image contrast due to compositional differences in atomic number, with increasing atomic number resulting in increased brightness. To further ensure that the increased brightness was due to the presence of barium, elemental composition was measured by electron probe microanalysis (EPMA) using energy dispersive spectroscopy (EDS) (INCA x-sight model 7636, Oxford Instruments America, Concord, MA). The relative intensity of Ba to Ca was compared between regions of high and low image brightness to verify that brightness differences were due to the presence of BaSO<sub>4</sub>.

The damaged area fractions, Dx.Ar.<sub>CT</sub> and Dx.Ar.<sub>H</sub> were compared between the loaded and unloaded groups by Wilcoxon's signed rank test, because the distributions were not normal. The median intensity of the bone voxels was compared between the three groups by ANOVA with Tukey's HSD post-hoc test. Linear regression was used to relate the bone peak median intensity and Dx.Ar.<sub>CT</sub> to Dx.Ar.<sub>H</sub>. All statistical analyses

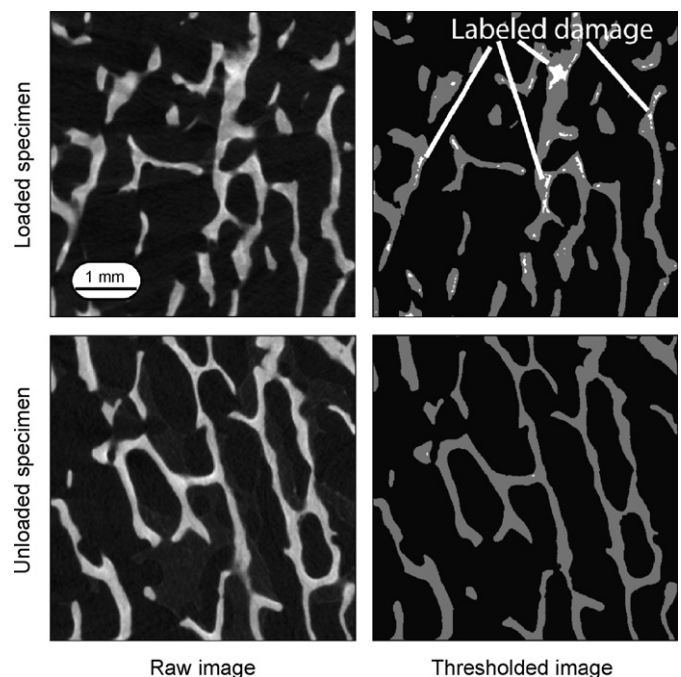


Fig. 2. Filtered (left) and thresholded micro-CT images from a loaded and an unloaded sample that were labeled with BaSO<sub>4</sub>. White regions in the thresholded images represent regions with higher attenuation labeled by BaSO<sub>4</sub>.

were performed with JMP IN version 5.1 (SAS Institute Inc., Cary, NC). The significance level for all tests was chosen as 0.05.

### 3. Results

Following processing, eight samples from group I, eleven from group II, and nine from group III remained for statistical analysis (Table 1).

All of the mechanically loaded specimens exhibited modulus reductions consistent with mechanical damage. The modulus decreased  $12.17 \pm 7.54\%$  (mean  $\pm$  std. dev.) after the compressive overload, indicating apparent level damage was induced. The initial Young's modulus was  $1089 \pm 464$  MPa vs.  $952 \pm 427$  MPa following mechanical loading ( $p < 0.001$ , paired *T*-test).

Microcracks were visible in the tissue matrix under both light microscopy and SEM. The mean histologically measured damaged area fraction was more than twice as high in the damaged group as in the undamaged group ( $p = 0.003$ , Fig. 4), verifying that damage resulted from the mechanical loading.

The micro-CT measurements of damage also indicated greater damage in the loaded group than the unloaded group. The median intensity of the bone tissue in the CT scans was approximately 6% higher in the loaded specimens than the unloaded specimens, indicating a higher uptake of BaSO<sub>4</sub> in the loaded samples ( $p = 0.01$ , Fig. 4). Consistent with this finding, the micro-CT measured damaged area fraction was more than 3.5 times higher in the damaged group than the undamaged group ( $p = 0.015$ ). Both the



micro-CT measured damage fraction ( $p = 0.02$ ,  $R^2 = 0.389$ ) and the median intensity ( $p = 0.04$ ,  $R^2 = 0.217$ ) were linearly correlated with the histologically measured damage (Fig. 5).

Changing the grid size for the histological crack counting increased the predicted damage area fraction. Hence, measurement of damage was sensitive to grid size. However, differences between the loaded and unloaded groups were significant for both grid sizes. The correlation coefficients between Dx.Ar.H vs. Dx.Ar.CT and the median intensity also decreased slightly to 0.379 and 0.210, respectively.

Several microcracks surrounded by regions of increased image brightness were evident in SEM (Fig. 6). EPMA verified that the difference in brightness was due to higher

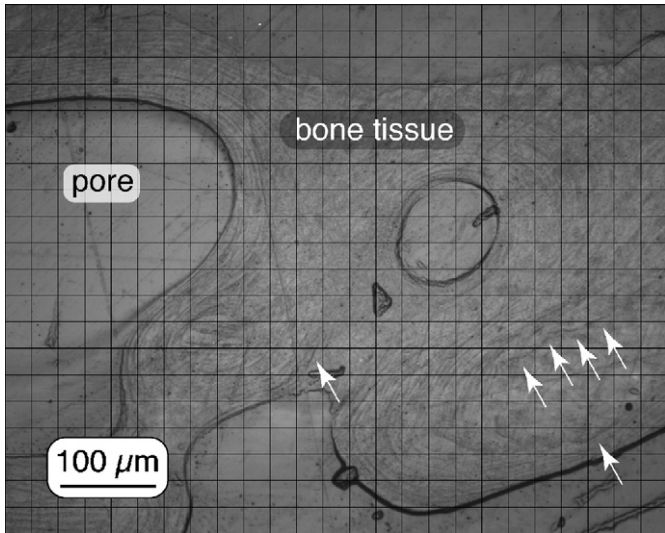


Fig. 3. A micrograph showing damaged areas (arrows). The damaged area fraction was calculated as the ratio of squares that contained microcracks to the total number of squares containing bone.

relative levels of barium in the bright regions, with an intensity ratio of Ba to Ca over four times higher at the locations near microcracks compared to adjacent undamaged regions. Microcracks that were not labeled by barium were also observed, which were assumed to be artifacts caused by drying and embedding.

4. Discussion

A non-destructive technique for detection of micro-damage in whole trabecular bone samples using micro-CT was developed. This technique, although lacking the precision of direct crack counting and measurement by histology, could allow an improved understanding of the three-dimensional relationship between damage and morphology. The positive linear regression between the median intensity and crack area and the correlation between the volume of high-intensity regions in the image and the measured damaged area fraction indicated that damaged regions were labeled by preferential precipitation of BaSO<sub>4</sub>, possibly due to increased porosity that provided surfaces for nucleation and formation of BaSO<sub>4</sub> particles. The new technique cannot quantify the traditional measures of microdamage such as crack density (Cr.Dn.), crack length (Cr.Ln.), or crack surface density (Cr.S.Dn.). However, it was capable of differentiating between undamaged and damage specimens, and provided a measure that was correlated to histologically measured damage. When applied to complete three-dimensional images, this non-destructive technique has the potential to identify damaged trabeculae based on the CT intensity in order to study the morphology and orientation of damaged vs. undamaged trabeculae under different loading scenarios.

Typical microcracks have an opening on the order of 1 μm, which is an order of magnitude lower than the

Table 1  
Summary of measured parameters

|                                     | Group                     |                          |                          |
|-------------------------------------|---------------------------|--------------------------|--------------------------|
|                                     | I                         | II                       | III                      |
| Description                         | Loaded and treated        | Unloaded and treated     | Control                  |
| N                                   | 8                         | 10                       | 9                        |
| Initial modulus (MPa)               | 1091 ± 410                |                          |                          |
| Damaged modulus (MPa)               | 965.6 ± 381               |                          |                          |
| Volume fraction (dimensionless)     | 0.225 ± 0.052             | 0.232 ± 0.056            | 0.205 ± 0.049            |
| Dx.Ar.H (%) small grid              | 1.06 ± 0.34 <sup>a</sup>  | 0.49 ± 0.34 <sup>a</sup> |                          |
| Dx.Ar.H (%) large grid              | 2.13 ± 0.51 <sup>a</sup>  | 1.04 ± 0.65 <sup>a</sup> |                          |
| Dx.Ar.CT (%)                        | 4.54 ± 2.94 <sup>a</sup>  | 1.23 ± 0.81 <sup>a</sup> | 0                        |
| Median CT intensity (dimensionless) | 18816 ± 1089 <sup>b</sup> | 17721 ± 593 <sup>b</sup> | 14336 ± 598 <sup>b</sup> |

Values are given as mean ± std. dev.  
Dx.Ar.H: Damaged area fraction quantified by area counting.  
Dx.Ar.CT: Damaged area fraction quantified by micro-CT imaging.  
<sup>a</sup> $p < 0.005$ , Wilcoxon signed rank test.  
<sup>b</sup> $p < 0.001$ , ANOVA with Tukey's HSD test.

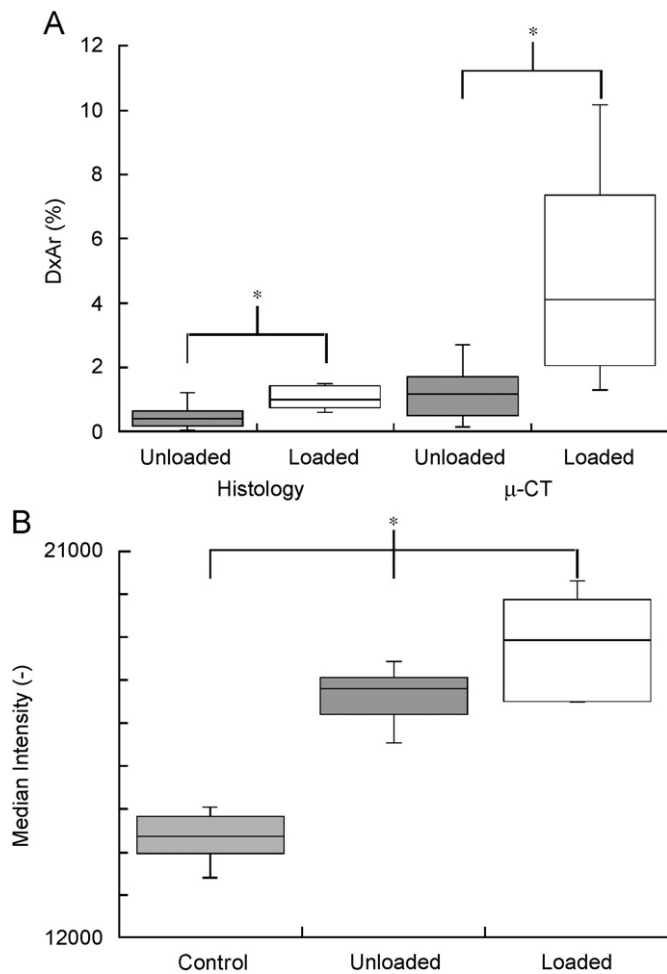


Fig. 4. (A) The mean damaged areas measured by both histology and by micro-CT were lower for the undamaged samples than for the damaged samples; (B) the BaSO<sub>4</sub> treated samples had higher median intensities than unlabeled control samples, and the loaded samples had a higher median intensity than the unloaded samples. (\*Indicates significant differences across groups  $p < 0.02$ .) The boxes in the plots bound the 25th and 75th percentiles of the data, while the bar indicates the range.

scanner resolution. However, the high X-ray attenuation of barium compared to bone, and the penetration of BaSO<sub>4</sub> into the tissue surrounding the damage, which was evident in SEM (Fig. 6), allowed the damage to be detected. These effects will result in an over estimation of the total damaged area, but can differentiate between bones with differing damage content.

The study has some notable strengths. Foremost, multiple measures were used to verify both macroscopic and microscopic damage presence in the samples. Second, linear regression was used to directly correlate the measures of damage from micro-CT with a histological technique. A parameter study was performed to ensure that the results were not an artifact of the grid size chosen for the histological measurements. From an experimental standpoint, the use of endcaps during testing reduced end effects (Keaveny et al., 1997). This testing protocol produces uniform damage patterns within the specimen cross section (Wang and Niebur, 2006; Wang et al., 2005).

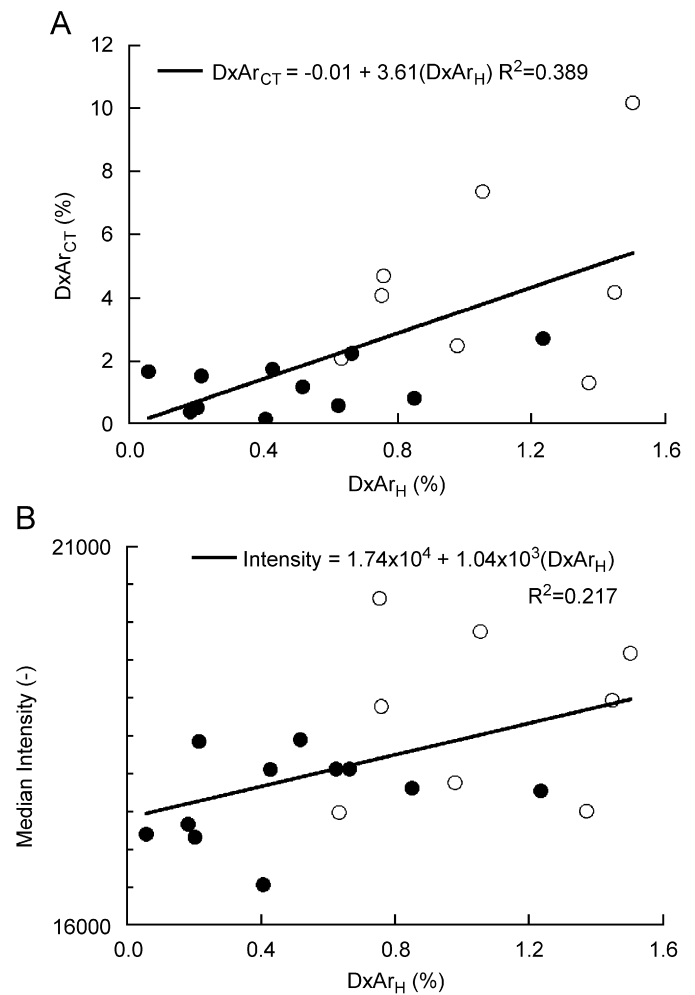


Fig. 5. The CT measured damage area fraction, DxA<sub>r,CT</sub>, ( $p < 0.005$ , A) and the median image intensity of the bone tissue ( $p < 0.04$ , B) were both correlated with the histologically measured damaged area fraction (DxA<sub>r,H</sub>). The open circles represent the specimens that were mechanically loaded, and the filled circles are specimens that were not loaded.

There are some limitations to this study. The primary advantage of this technique is expected to be the analysis of three-dimensional damage patterns, but that was not exploited in this initial study. Instead, the initial focus was to verify the capability of the method to detect damage. However, as a result, the capability to identify the morphology of damaged trabeculae or otherwise relate damage to microstructure could not be confirmed. Second, the histological measurements would have been improved, had a stain such as basic fuchsin or alizarin been applied to the samples before dehydration and imaging. However, the BaSO<sub>4</sub> treatment may have interfered with the staining, as fuchsin also relies on precipitation within void spaces, and alizarin or other such chelating agents may also chelate to barium. Finally, the alignment of the specimens with respect to the trabecular architecture was not controlled (Wang et al., 2004). Any such misalignment would have had a minor effect in this study, but would be important to understand relationships between damage, loading mode, and trabecular architecture.

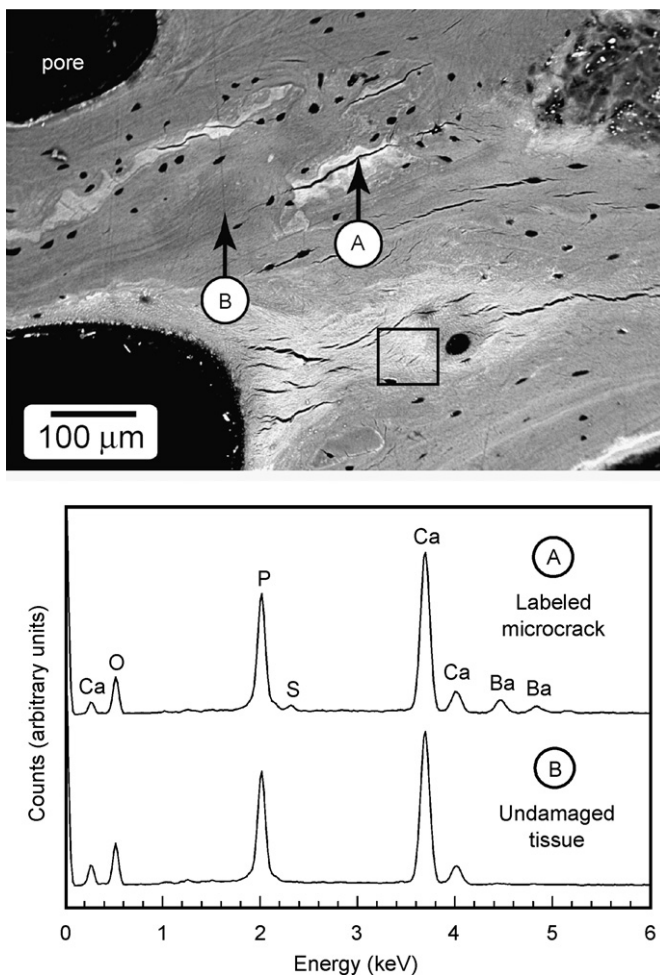


Fig. 6. A backscattered SEM image of a loaded and treated specimen showed several microcracks surrounded by bright regions. The square surrounds a region with several adjacent cracks less than 5  $\mu\text{m}$  in length, which would appear histologically as diffuse damage. EDS was used to measure the elemental composition, which verified that the bright region labeled A contained a higher level of barium than the region labeled B. Cracks that are not labeled with  $\text{BaSO}_4$  were considered to be artifacts caused by drying and embedding the sample for SEM imaging.

Lead sulfide ( $\text{PbS}$ ) has previously been used as a contrast agent to enhance detection of microdamage in bone by back-scattered SEM (Schaffler et al., 1994). Based on the same principle employed here, individual microcracks and diffuse damage were labeled by precipitation of  $\text{PbS}$  into void spaces in the bone. The labeled regions were detected by their increased brightness in SEM, and could be visually differentiated as microcracks, diffuse damage, or anatomic features such as Haversian canals and lacunae. The limited resolution and the large volumetric data sets make it impossible to distinguish damage morphology in this way in micro-CT. However, the advantages of the micro-CT technique are the potential to image large regions and assess the three-dimensional distribution of damage with respect to the trabecular architecture and a less hazardous chemical composition.

The area counting protocol used to measure damage only gave a relative measure of the “damaged area” in a

section. Such point and area counting techniques are common for the assessment of damage in bone, because they provide a tractable method for comparing damage levels in bones of differing loading or health histories (Fazzalari et al., 2002). To ensure that the choice of grid size did not obscure or artificially create differences in the data that did not exist, two different grid sizes were applied to the damage measurements. This analysis was not intended to verify that the area counting technique gave a true value of the damaged area, but rather to show that the correlations between the histological measurement and the micro-CT measurements were not artifacts of the grid size. The loaded samples had a larger damaged area fraction than the unloaded samples for both grid sizes, indicating that relative differences in damage levels were captured in both cases. The strength and significance of the regressions were similarly unaffected, although the coefficients were different. Hence, although both grids only approximated the true damaged area, the agreement between the two grid sizes demonstrates that the results were not an artifact of grid size.

The presence of microdamage in the unloaded specimens was probably an artifact of drying and embedding. In previous studies almost no microdamage was found in bovine trabecular bone specimens that were not subjected to mechanical loading (Arthur Moore and Gibson, 2002; Wachtel and Keaveny, 1997; Wang and Niebur, 2006; Wang et al., 2005). It is possible that the cracks in the undamaged specimens developed during specimen preparation,  $\text{BaSO}_4$  precipitation, dehydration, or embedding. When using basic fuchsin staining to label microdamage, visible microcracks that are not labeled are assumed to be artifactual (Burr and Stafford, 1990). As such, the presence of cracks that did not contain  $\text{BaSO}_4$  in the SEM image (Fig. 6) suggests that at least some cracks were indeed the result of drying and embedding. This artifactual damage would not be detected in the micro-CT image due to the absence of barium.

The increase in the median intensity in the undamaged specimens relative to the controls was not believed to be due to pre-existing damage in the samples, but rather to precipitation of  $\text{BaSO}_4$  in lacunae and canaliculae and leaching of barium into the tissue matrix. In practice, a small control group would allow the increased intensity to be quantified so that an appropriate threshold could be selected.

The inclusion of diffuse damage in the micro-CT damaged area fraction but not in the histological measurements could have negatively impacted the correlation between the two methods. Loading to 3% apparent compressive strain is known to form both microcracks and diffuse microdamage in trabecular bone (Arthur Moore and Gibson, 2002; Wang and Niebur, 2006; Wang et al., 2005). Diffuse damage labeled by  $\text{BaSO}_4$  was evident around groups of small cracks when viewed under back-scattered SEM (Fig. 6), and the thresholded images also showed focal uptake of  $\text{BaSO}_4$ . However, because no



labeling agents were used for the histology, diffuse damage was not detectable in the thin sections and hence could not be considered in the correlations.

The resolution of commercial micro-CT scanning systems does not allow this method to precisely image microcracks. As such, the technique is currently most powerful as a complement to microscopic techniques. However, synchrotron CT imaging can be performed at a resolution of 1  $\mu\text{m}$  or less (Kinney et al., 2000; Thurner et al., 2006), and recently desktop scanners with sub-micron resolution have become available. While these systems will allow detailed visualization of individual microcracks, detecting damaged regions could be enhanced by the use of appropriate contrast agents.

### Conflict of interest

None of the authors have financial or personal interests with organizations that may benefit from this work.

### Acknowledgment

This research was supported by the National Institutes of Health awards AR049598 and AR052008.

### References

- Arthur Moore, T.L., Gibson, L.J., 2002. Microdamage accumulation in bovine trabecular bone in uniaxial compression. *Journal of Biomechanical Engineering* 124, 63–71.
- Burr, D.B., Stafford, T., 1990. Validity of the bulk-staining technique to separate artifactual from in vivo bone microdamage. *Clinical Orthopaedics*, 305–308.
- Burr, D.B., Martin, R.B., Schaffler, M.B., Radin, E.L., 1985. Bone remodeling in response to in vivo fatigue microdamage. *Journal of Biomechanics* 18, 189–200.
- Fazzalari, N.L., Forwood, M.R., Manthey, B.A., Smith, K., Kolesik, P., 1998. Three-dimensional confocal images of microdamage in cancellous bone. *Bone* 23, 373–378.
- Fazzalari, N.L., Kuliwaba, J.S., Forwood, M.R., 2002. Cancellous bone microdamage in the proximal femur: influence of age and osteoarthritis on damage morphology and regional distribution. *Bone* 31, 697–702.
- Frost, H.M., 1960. Presence of microscopic cracks in vivo in bone. *Bull Henry Ford Hospital* 8, 27–35.
- Keaveny, T.M., Wachtel, E.F., Guo, X.E., Hayes, W.C., 1994. Mechanical behavior of damaged trabecular bone. *Journal of Biomechanics* 27, 1309–1318.
- Keaveny, T.M., Pinilla, T.P., Crawford, R.P., Kopperdahl, D.L., Lou, A., 1997. Systematic and random errors in compression testing of trabecular bone. *Journal of Orthopaedic Research* 15, 101–110.
- Kinney, J.H., Haupt, D.L., Balooch, M., Ladd, A.J., Ryaby, J.T., Lane, N.E., 2000. Three-dimensional morphometry of the l6 vertebra in the ovariectomized rat model of osteoporosis: biomechanical implications. *Journal of Bone and Mineral Research* 15, 1981–1991.
- Lee, T.C., Myers, E.R., Hayes, W.C., 1998. Fluorescence-aided detection of microdamage in compact bone. *Journal of Anatomy* 193 (Pt 2), 179–184.
- Lee, T.C., Mohsin, S., Taylor, D., Parkesh, R., Gunnlaugsson, T., O'Brien, F.J., Giehl, M., Gowin, W., 2003. Detecting microdamage in bone. *Journal of Anatomy* 203, 161–172.
- Morgan, E.F., Yeh, O.C., Chang, W.C., Keaveny, T.M., 2001. Nonlinear behavior of trabecular bone at small strains. *Journal of Biomechanical Engineering* 123, 1–9.
- O'Brien, F.J., Taylor, D., Dickson, G.R., Lee, T.C., 2000. Visualisation of three-dimensional microcracks in compact bone. *Journal of Anatomy* 197 (Pt 3), 413–420.
- Parkesh, R., Gowin, W., Lee, T.C., Gunnlaugsson, T., 2006. Synthesis and evaluation of potential CT (computer tomography) contrast agents for bone structure and microdamage analysis. *Organic and Biomolecular Chemistry* 4, 3611–3617.
- Scanco, 1999. *Scanco Micro-CT Users Manual*. Bassersdorf, Switzerland.
- Schaffler, M.B., Pitchford, W.C., Choi, K., Riddle, J.M., 1994. Examination of compact bone microdamage using back-scattered electron microscopy. *Bone* 15, 483–488.
- Thurner, P.J., Wyss, P., Voide, R., Stauber, M., Stampanoni, M., Sennhauser, U., Muller, R., 2006. Time-lapsed investigation of three-dimensional failure and damage accumulation in trabecular bone using synchrotron light. *Bone* 39, 289–299.
- Wachtel, E.F., Keaveny, T.M., 1997. Dependence of trabecular damage on mechanical strain. *Journal of Orthopaedic Research* 15, 781–787.
- Wang, X., Niebur, G.L., 2006. Microdamage propagation in trabecular bone due to changes in loading mode. *Journal of Biomechanics* 39, 781–790.
- Wang, X., Liu, X., Niebur, G.L., 2004. Preparation of on-axis cylindrical trabecular bone specimens using micro-CT imaging. *Journal of Biomechanical Engineering* 126, 122–125.
- Wang, X.S., Guyette, J., Liu, X., Roeder, R.K., Niebur, G.L., 2005. Axial-shear interaction effects on microdamage in bovine tibial trabecular bone. *European Journal of Morphology* 42, 61–70.

# Functionalized gold nanoparticles as an x-ray contrast agent for bone microdamage

Ryan Ross, Zhenyuan (Mark) Zhang, Ryan Roeder

During normal repetitive loading, stresses in bone can cause damage in the form of microcracks and diffuse damage [1,2]. Normally these microcracks stimulate a cellular remodeling process [2]. During this remodeling process, osteoclasts resorb the damaged bone regions while osteoblasts lay new bone material in its place repairing the damaged regions [3]. However, situations can arise where the damage and remodeling processes are no longer in equilibrium. In active individuals, such as athletes or military recruits, damage may accumulate too quickly for the remodeling process to repair. Another example is in elderly individuals where the remodeling process has been impaired [4]. Additionally, pharmacological treatments for bone diseases such as osteoporosis attempt to diminish bone remodeling in order to preserve bone mass. However, the accumulation of microcracks may be an unintended and detrimental consequence of the treatment. *In vivo* fatigue microdamage has been shown to correlate with a degradation of mechanical properties [1]. Loss of stiffness and a decrease in fracture toughness are common in damaged tissue, which leads to increased risk of fracture in damaged regions [1]. The process by which microcracks develop, propagate and ultimately lead to a failure *in vivo*, is poorly understood due to an inability to detect microdamage *in vivo*.

Current techniques for imaging microdamage, such as UV-light microscopy after staining with fluorochromes, are inherently destructive and two-dimensional. Non-destructive, three-dimensional imaging was recently facilitated using computed tomography and a precipitated barium sulfate stain, but the stain was not damage specific and not biocompatible [5,6]. Therefore, functionalized gold nanoparticles (AuNPs) were investigated as a biocompatible x-ray contrast agent. AuNPs were chosen due to the particles relative stability, ease of surface functionalization, and increased X-ray attenuation relative to bone mineral.

AuNPs were synthesized using a citrate reduction reaction and surface functionalized with glutamic acid, in order to facilitate damage specific binding through carboxylic acid side groups. Once functionalized with glutamic acid, the particles were evaluated for stability in solution, specificity to damage, deliverability, and x-ray attenuation. Dynamic light scattering experiments (DLS) and TEM images proved that synthesized particles were stable below 30nm. Initial tests demonstrate that functionalized AuNPs were able to selectively target artificially damaged regions in bone, using both atomic force microscopy (AFM) and backscattered electron imaging coupled with energy-dispersive X-ray spectroscopy (BSEI-EDXA).

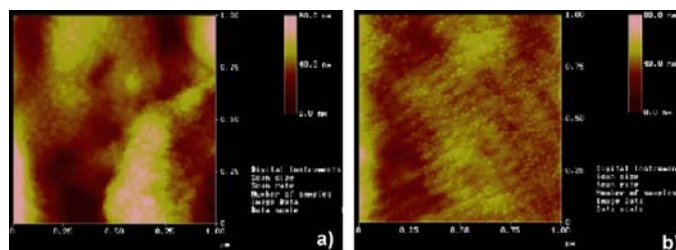


**Figure 1:** Atomic force microscopy (AFM) images: a) outside of cracked region no particles are present while b) inside cracked region particles can be detected.

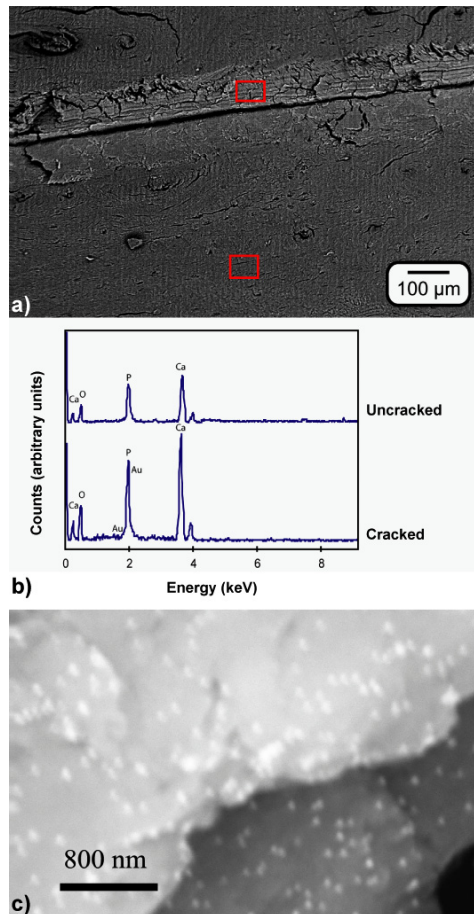


**Figure 2:** BSEI-EDXA data: a) The regions investigated with EDXA. b) EDXA data of regions both inside and outside cracked area shows peaks for the presence of atomic gold within the cracked regions. c) Cracked regions under higher magnification shows the presence of gold particles.

- [1] Tami AE, Nasser P, Schaffler MB, Knothe Tate ML. Noninvasive fatigue fracture model of the rat ulna. *Journal of Orthopaedic Research* 2003;21:1018-1024.
- [2] Parkesh R, Mohsin S, Lee TC, Gunnlaugsson T. Histological, spectroscopic, and surface analysis of microdamage in bone: toward real-time analysis using fluorescent sensors. *Chemistry of Materials* 2007;19:1656-1663.
- [3] Parkesh R, Lee TC, Gunnlaugsson T, Gowin W. Microdamage in bone: surface analysis and radiological detection. *Journal of Biomechanics* 2006;39:1552-1556.
- [4] Lee TC, Mohsin S, Taylor D, Parkesh R, Gunnlaugsson T, O'Brien FJ, Giehl M, Gowin W. Detecting microdamage in bone. *Journal of Anatomy* 2003;203:161-172.
- [5] Leng W, Wang X, Ross RD, Niebur GL and Roeder RK. Micro-computed tomography of fatigue microdamage in cortical bone using a barium sulfate contrast agent. *Journal of the Mechanical Behavior of Biomedical Materials* 2008;1:68-75.
- [6] Leng H, Wang X, Niebur GL, Roeder RK. Synthesis of a barium sulfate nanoparticle contrast agent for micro-computer tomography of bone microstructure. *Ceramic Transactions* 2004;159:219-229.

**SBC2007-175238**

**SYSTEMATIC ERROR IN THE MEASURE OF MICRODAMAGE BY MODULUS  
DEGRADATION DURING FOUR-POINT BENDING FATIGUE**

**Matthew D. Landrigan, Ryan K. Roeder**

Department of Aerospace and Mechanical Engineering  
University of Notre Dame  
Notre Dame, IN 46556  
Email: rroeder@nd.edu

**INTRODUCTION**

The accumulation of fatigue damage in bovine and human cortical bone is conventionally measured by modulus or stiffness degradation. The initial modulus or stiffness of each specimen is typically measured in order to normalize tissue heterogeneity to a prescribed strain [1,2]. Cyclic preloading at 100 N for 20 cycles has been used for this purpose in both uniaxial tension and four-point bending tests [1-3]. In four-point bending, the specimen modulus is often calculated using linear elastic beam theory as,

$$E = \frac{3Fl}{4bh^2\varepsilon} \quad (1)$$

where  $F$  is the applied load,  $l$  is the outer support span,  $b$  is the specimen width,  $h$  is the specimen height, and  $\varepsilon$  is the maximum strain based on the beam deflection [2]. The maximum load and displacement data from preloading is used to determine the initial specimen modulus. The initial modulus and a prescribed maximum initial strain are then used to determine an appropriate load for fatigue testing under load control.

The goal of this study was to determine the effect of the preload on the calculation of the initial specimen modulus and the amount of damage accumulation during fatigue testing. Bovine cortical bone beams were tested in four-point bending to measure the initial specimen modulus at varying levels of load. Fatigue tests were conducted at the same prescribed level of strain but based on two different measures of the initial specimen modulus.

**METHODS**

Ten parallelepiped beams, nominally 4 x 4 x 50-60 mm, were prepared on a CNC mini-mill (Sherline CNC Mill 5400) after

harvesting tissue from two bovine tibiae and randomly assigned to two groups. Specimens were wrapped in gauze, hydrated, and stored at -20°C in airtight containers during interim periods.

All mechanical tests were performed with the periosteal specimen surface in tension in cyclic four-point bending (20 and 40 mm inner and outer span, respectively) on an electromagnetic test instrument (BOSE ElectroForce 3300). Measurements of the initial specimen modulus were conducted in de-ionized water at room temperature. Group A was loaded at 2 Hz with a minimum load of 4 N and the maximum load increased by 20 N from 40 to 300 N every 30 cycles. The maximum load in group B decreased by 20 N from 300 to 40 N every 30 cycles. The initial specimen modulus was calculated from the maximum load and displacement data using Eq. 1.

Specimens in groups A and B were then randomly reassigned to groups 1 and 2. Both groups were tested in four-point bending fatigue under load control at 2 Hz in phosphate buffered saline at 37°C. The applied load for specimens in groups 1 and 2 was normalized to 6000  $\mu$ strain [4] using the initial specimen modulus determined at preload of 100 N and 200 N, respectively. Tests were concluded at 400,000 cycles without failure.

Experimental groups were compared using analysis of variance (ANOVA) with a level of significance of 0.05 (StatView). Nonlinear regression was used to correlate the initial specimen modulus with the applied load by a power-law relationship and the modulus degradation with the number of loading cycles by a second order polynomial. Analysis of covariance (ANCOVA) was used to compare regressions between groups.

**RESULTS**

The initial specimen modulus increased with increasing applied load following a power-law relationship modulus (Fig. 1). Groups A

and B were not statistically different ( $p = 0.33$ , ANOVA) indicating that damage was not accumulated during the preloading experiment. Thus, variation was simply due to specimen heterogeneity and the specimens were randomly reassigned to groups 1 and 2 for fatigue testing. Specimens that were loaded based on conditions determined by measuring the initial specimen modulus at a 200 N preload exhibited a 31% loss in modulus compared to a 19% loss in modulus for specimens preloaded at 100 N ( $p < 0.0001$ , T-test) after 400,000 cycles (Fig. 2). The overall difference between the two groups was also statistically significant ( $p < 0.0001$ , ANCOVA).

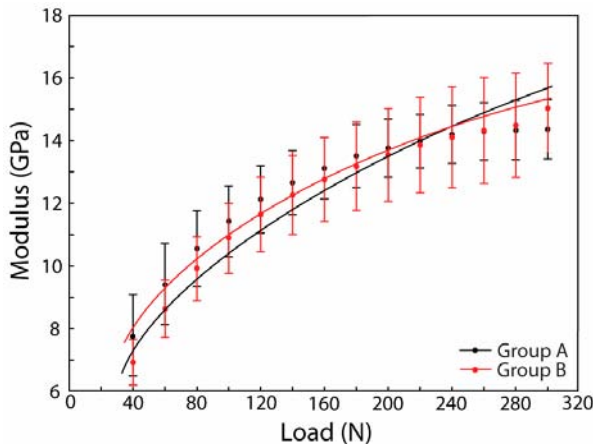


**Figure 1. The dependence of the initial beam modulus on the magnitude of the applied preload for specimens loaded from 40 to 300 N (Group A) and 300 to 40 N (Group B). The mean ( $\pm$  standard deviation) is shown for each load. Data was fit by nonlinear regression using a power-law ( $R^2 = 0.78$  and  $0.80$  for groups A and B, respectively).**

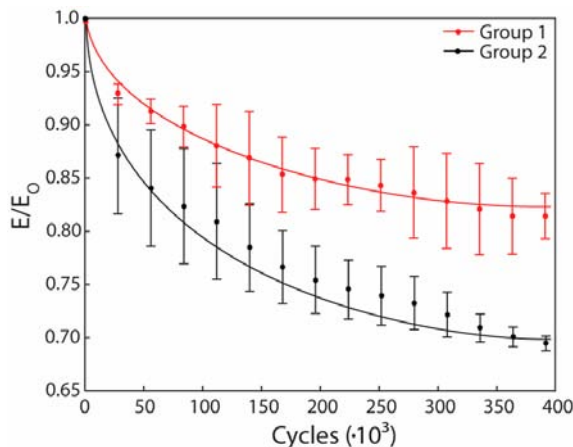


**Figure 2. Modulus degradation during load-controlled four-point bending fatigue of specimens normalized to an initial maximum strain of  $6000 \mu\text{strain}$  using an initial specimen modulus determined at a 100 N (Group 1) and 200 N (Group 2) preload. The mean ( $\pm$  standard deviation) is shown for each group. Data was fit by nonlinear regression using a second order polynomial ( $R^2 = 0.69$  and  $0.79$  for groups 1 and 2, respectively).**

## DISCUSSION

Four-point bending fatigue specimens that were normalized by measuring the initial specimen modulus at 200 N experienced a 63% greater loss in modulus than the specimens normalized at 100 N. The higher initial specimen modulus (measured at 200 N) had the greatest effect on the modulus degradation during the first 10% of the fatigue test. After 80,000 cycles, the specimens normalized from the 200 N preload exhibited the same modulus degradation as those normalized at 100 N did in 400,000 cycles. Therefore, the selection of a preload for measuring the initial specimen modulus causes systematic error in the measurement of modulus degradation.

Due to the viscoelastic nature of bone, intrinsic errors exist in using a preload fatigue protocol to measure the initial specimen modulus. The modulus was nonlinearly dependent on the magnitude of the preload when calculated from Eq. 1 (Fig. 1). The magnitude of the initial specimen modulus measured using a preload of 200 N was 19% higher than that measured using a preload of 100 N. The 100 N preload was likely chosen originally for uniaxial tension tests where a uniform stress distribution results in a low stress level. In four-point bending, the maximum stress is an order of magnitude higher than in uniaxial tension negating the benefits of low-level preload test.

The loading and unloading portions of the load displacement curve are not linear for a viscoelastic material. Use of the maximum load and displacement data to determine the initial specimen modulus was shown to be nonlinear. Another important consideration is the use of alternative methods available for calculating the modulus or stiffness. The secant modulus, defined as the slope of the line connecting the endpoints of the load displacement curve, has been used previously [5] which would eliminate the effects of plastic strain. The specimen stiffness is another method where the slope of the loading portion of the load displacement curve is computed by a least squares approximation [6]. A systematic evaluation of the use of these methods for measuring the initial specimen modulus and the modulus degradation during fatigue is underway.

## ACKNOWLEDGEMENT

This research was supported by the U.S. Army Medical Research and Materiel Command (W81XWH-06-1-0196).

## REFERENCES

1. Diab, T., and Vashishth, D., 2005, "Effects of damage morphology on cortical bone fragility," *Bone*, Vol. 37, pp. 96-102.
2. Boyce, T. M., Fyhrie, D. P., Glotkowski, M. C., Radin, E. L., and Schaffler, M. B., 1998, "Damage Type and Strain Mode Associations in Human Compact Bone Bending Fatigue," *Journal of Orthopaedic Research*, Vol. 16, pp. 322-329.
3. Cotton, J. R., Winwood, K., Zioupos, P., and Taylor, M., 2005, "Damage Rate is a Predictor of Fatigue Life and Creep Strain Rate in Tensile Fatigue of Human Cortical Bone Samples," *Journal of Biomechanical Engineering*, Vol. 127, pp. 213-219.
4. Currey, J. D., 2004, "Tensile Yield in Compact Bone is Determined by Strain, Post-yield Behavior by Mineral Content," *Journal of Biomechanics*, Vol. 37, pp. 549-556.
5. Pattin, C. A., Caler, W. E., and Carter, D. R., 1996, "Cyclic Mechanical Property Degradation During Fatigue Loading of Cortical Bone," *Journal of Biomechanics*, Vol. 29, pp. 69-79.
6. Burr, D. B., Turner, C. H., Naick, P., Forwood, M. R., Ambrosius, W., Hasan, M. S., and Pidaparti, R., 1998, "Does Microdamage Accumulation Affect the Mechanical Properties of Bone," *Journal of Biomechanics*, Vol. 31, pp. 337-345.



# Functionalized Gold Nanoparticles as a Damage Specific Contrast Agent for Bone

Zhenyuan Zhang, Ryan D. Ross, and Ryan K. Roeder.

Department of Aerospace and Mechanical Engineering, University of Notre Dame, Notre Dame, IN 46556.

**Introduction:** Accumulation of microdamage in bone tissue can lead to an increased risk of fracture, including stress fractures in active individuals and fragility fractures in the elderly. Current methods for detecting and imaging microdamage are inherently invasive. Therefore, micro-computed tomography (micro-CT) was proposed and demonstrated using precipitated  $\text{PbS}^1$  or  $\text{BaSO}_4^{2,3}$  as a non-specific contrast agent. The objective of this study was to improve specificity and deliverability by preparing functionalized gold nanoparticles (Au NPs) as a new contrast agent. Au NPs with a mean diameter of 20 and 40 nm were synthesized and functionalized with L-glutamic acid. Au NPs are well known to have affinity with carboxy, amine, and thiol groups.

**Methods:** Au NPs were synthesized from  $\text{HAuCl}_4 \cdot 3\text{H}_2\text{O}$  (Aldrich) and sodium citrate following the method developed by Turkevich and co-workers.<sup>4,5</sup> The obtained sol was wine red and the concentration was adjusted to approximately 0.5 mM. Au NPs were functionalized with L-glutamic acid (Fig. 1). 236 mL of the Au solution was mixed with 14 mL 2% poly(vinyl alcohol) (PVA, Aldrich,  $M_w = 50,000\text{--}85,000$ ) and then 5.8 g ion exchange resin (Sigma, Amberlite MB-150) was added to the mixture to remove citrate ions. After stirring overnight, 3 mL 0.72 mM L-glutamic acid was added and stirred for 3 days to functionalize the Au NP surface. The amount corresponded to one monolayer of glutamic acid on the Au NP surface assuming a surface coverage of  $40 \text{ \AA}^2$  per amine group. Au NPs were also synthesized by  $\text{NaBH}_4$  reduction<sup>6</sup> and functionalized with one monolayer of glutamic acid using methods similar to those described above. Au NPs synthesized by either method were characterized by UV-Vis spectroscopy (Cary 50 Bio UV-Vis Spectrophotometer) and Dynamic Light Scattering (DLS, Malvern Zetasizer Nano ZS).

Six bovine cortical bone specimens ( $12 \times 5 \times 5$  mm) were soaked in 0.5 mM calcein for 1.5 h under vacuum to stain damage from specimen preparation. Specimens were scratched with a scalpel to create new damage and soaked in solutions containing functionalized Au NPs for 24 h.

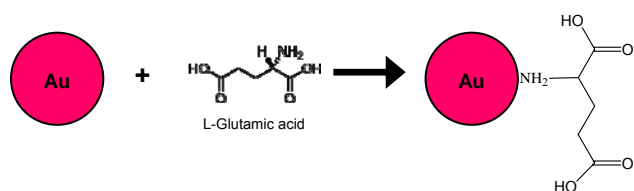


Figure 1. Strategy to functionalize Au NPs

**Results/Discussion:** Au NPs synthesized by citrate and  $\text{NaBH}_4$  reduction were measured to have a mean size of approximately 20 and 40 nm, respectively as determined by DLS (Fig. 2). The characteristic plasmon bands of Au NPs were observed in UV-Vis spectra (Fig. 3). The peak

positions were 516 nm and 534 nm for 20 and 40 nm Au NPs, respectively. The plasmon band position was unchanged after functionalization indicating that the Au NPs were dispersed. Scratches created on the surface of bone specimens were visibly stained red by the functionalized Au NPs (Fig. 4). Future work will investigate the feasibility of imaging the Au NPs by micro-CT.

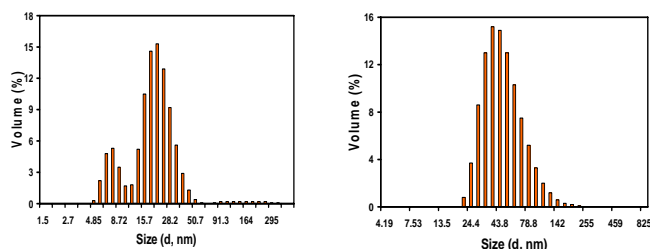


Figure 2. Particle size distribution measured by DLS for Au NPs synthesized by citrate (left) and  $\text{NaBH}_4$  (right) reduction.

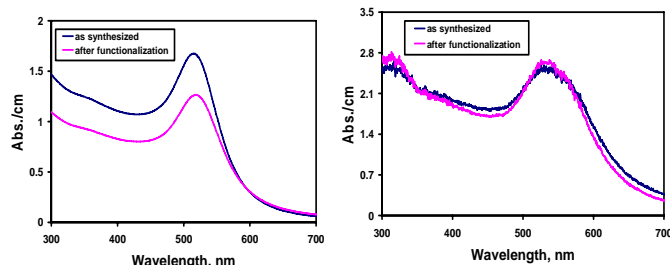


Figure 3. UV-Vis spectra of Au NPs synthesized by citrate (left) and  $\text{NaBH}_4$  (right) reduction before (blue) and after (pink) functionalization with L-glutamic acid.



Figure 4. Optical micrograph showing scratches on the surface of a bone specimen stained by Au NPs (dark). The width of the specimen is 5 mm.

**Conclusions:** Au NPs were synthesized, functionalized with L-glutamic acid, and demonstrated to bind to damage in bone.

**Acknowledgement:** USAMRMC W81XWH-06-1-0196

## References:

1. Leng H. et al. Trans. Orthop. Res. Soc. 2005;30:665.
2. Masse DB. et al. Trans. Orthop. Res. Soc. 2005;30:35.
3. Leng H. et al. Biomaterials 2006 submitted
4. Turkevich J. et al. Discuss. Faraday Soc. 1951;11:55-75.
5. Enustun BV. et al. J. Am. Chem. Soc. 1963;85:3317-3328.
6. Lee PC. et al. J. Phys. Chem. 1982;86:3391-3395.



# Precipitation of a Barium Sulfate Nanoparticle Contrast Agent Using Microemulsions

Matthew J. Meagher\*, Zhenyuan Zhang<sup>†</sup> and Ryan K. Roeder<sup>†</sup>

\*Department of Chemical & Biomolecular Engineering, <sup>†</sup>Department of Aerospace & Mechanical Engineering  
University of Notre Dame, Notre Dame, IN 46556



Biomechanics & Biomaterials in Orthopaedics

http://www.nd.edu/~amebio

## Introduction

- Accumulation of microdamage in bone leads to an increased risk of fracture [1].
- Micro-computed tomography (Micro-CT) enables non-destructive detection of microdamage in bone tissue using a suitable contrast agent [2,3].
- Barium sulfate (BaSO<sub>4</sub>) nanoparticles, due to their small size, demonstrated biocompatibility and high x-ray attenuation have potential as a suitable contrast agent in bone [4].
- Therefore, the objective of this study was to synthesize dispersed BaSO<sub>4</sub> nanoparticles using microemulsions.

## Microemulsion Thermodynamics

- The thermodynamics of water in oil microemulsions (Fig. 1) allow for precise control of the droplet size providing a stable reaction template for the synthesis of nanoparticles by limiting agglomeration and controlling crystal growth [5-7].

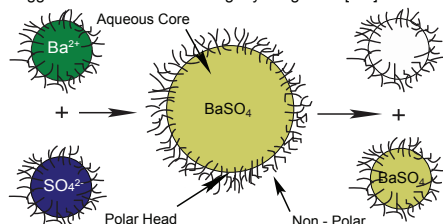


Fig. 1. Schematic diagram showing solute transfer between microemulsion droplets. The surfactant stabilized aqueous droplets suspended in the oil phase limit agglomeration by preventing precipitated nanoparticles from contacting each other, and control crystal growth by limiting the concentration of Ba<sup>2+</sup> and SO<sub>4</sub><sup>2-</sup> available for the reaction.

## Nanoparticle Synthesis

- Two microemulsions were prepared by adding 1.6 vol% of either a 0.1 M barium chloride or ammonium sulfate salt solution to a mixture of 90 vol% cyclohexane and a 10 vol% blend, containing Triton X-100 and hexanol in a 4:1 ratio by weight [7-10].
- Well-conditioned, isotropic microemulsions exhibited uniform droplet diameters, evidenced by optical clarity and decreased viscosity [7-10]. Dynamic light scattering (DLS, Malvern Zetasizer Nano-ZS) was used to measure the droplet size distribution (Fig. 2).
- The two microemulsions were added together and stirred vigorously for 90 min, allowing the contents of droplets to be exchanged and precipitate BaSO<sub>4</sub> nanoparticles (Fig. 1).
- Within the microemulsion droplets, BaSO<sub>4</sub> nanoparticles were synthesized via a simple precipitation reaction involving barium chloride and ammonium sulfate:  
$$\text{BaCl}_2(\text{aq}) + (\text{NH}_4)_2\text{SO}_4(\text{aq}) \rightarrow \text{BaSO}_4(\text{ppt}) + 2\text{NH}_4\text{Cl}(\text{aq})$$
- The microemulsion containing BaSO<sub>4</sub> was broken by evaporation; particles were collected by centrifugation, washed in ethanol and dispersed in cyclohexane.

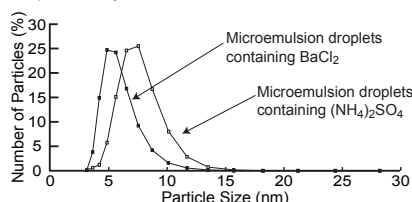


Fig. 2. DLS size distributions of microemulsion droplets containing barium chloride (BaCl<sub>2</sub>) and ammonium sulfate ((NH<sub>4</sub>)<sub>2</sub>SO<sub>4</sub>) salt solutions.

## Nanoparticle Characterization

- DLS was used to measure the droplet size distribution of the BaSO<sub>4</sub> microemulsion and the particle size distribution of BaSO<sub>4</sub> nanoparticles collected from the microemulsion (Fig. 3). Particle size distributions for BaSO<sub>4</sub> nanoparticles in the microemulsion and dispersed in cyclohexane showed that nearly all synthesized particles were less than 15 nm in diameter.
- Transmission electron microscopy (TEM, Hitachi H-600 Electron Microscope) was used to characterize the size and morphology of the BaSO<sub>4</sub> nanoparticles (Fig. 5). The nanoparticles appeared spherical, monosized, and well-dispersed.
- X-ray diffraction (XRD, X1 Advanced Diffraction System, Scintag, Inc.) was used to verify the crystallographic phase of the nanoparticles (Fig. 5).

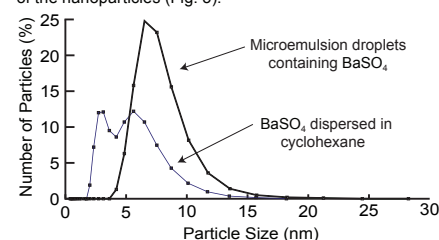


Fig. 3. DLS size distributions of microemulsion droplets containing BaSO<sub>4</sub> and BaSO<sub>4</sub> nanoparticles dispersed in cyclohexane.

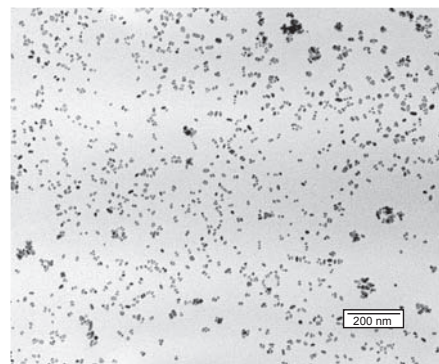


Fig. 4. TEM micrograph of the as-synthesized BaSO<sub>4</sub> nanoparticles.

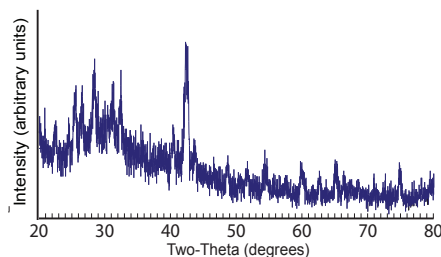


Fig. 5. XRD pattern of as-synthesized BaSO<sub>4</sub> nanoparticles. All peaks correspond to BaSO<sub>4</sub> (JCPDS 24-1035).

## Nanoparticle Dispersion

- BaSO<sub>4</sub> nanoparticles readily agglomerated once removed from the stabilizing environment of the microemulsion and redispersed in polar solvents such as water.
- A stable dispersion requires that the repulsive forces of the electrokinetic potential are large enough to overcome the attractive Van der Waals forces, which can be accomplished by altering the nanoparticle's surface charge by changing the pH of the dispersing solution. Electrokinetic potentials above 25 mV are typically reported for well-dispersed BaSO<sub>4</sub> [12,13].
- The zeta potential of BaSO<sub>4</sub> was measured (Malvern Zetasizer Nano-ZS) from natural to basic pH through titration with sodium hydroxide (NaOH) (Fig. 6). Despite a zeta potential above 25 mV for pH ≥ 8, the particles continued to agglomerate.

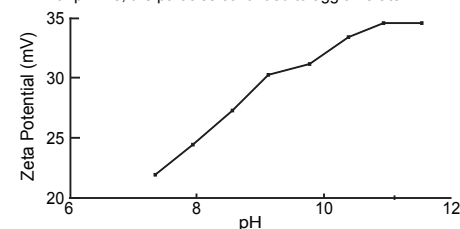


Fig. 6. The zeta potential (mV) of BaSO<sub>4</sub> nanoparticles increased with increasing pH.

## Summary

- BaSO<sub>4</sub> nanoparticles were synthesized via water in oil microemulsions as a potential contrast agent for x-ray imaging. Microemulsions enabled synthesis of BaSO<sub>4</sub> nanoparticles less than 15 nm in diameter. The BaSO<sub>4</sub> nanoparticles were dispersed in a non-aqueous solvent, but dispersion of the nanoparticles in an aqueous medium will require further work.

## Future Work

- Polyelectrolytes have been used in other particle processing applications to stabilize particle suspensions. Several polyelectrolyte molecules (e.g. PAA, PDADMAC, PAA-PEO) have been shown to bind to nanoparticles in suspension, coating them with a uniform charge that serves to stabilize the particle dispersions.
- Dextran coatings have been used to stabilize super-paramagnetic iron oxide nanoparticles for MRI. Being hydrophilic, if dextran adheres to the surface of the BaSO<sub>4</sub>, the nanoparticles may be dispersed in an aqueous solution [14,15].

## Acknowledgements

This research was supported by the U.S. Army Medical Research and Materiel Command (W81XWH-06-1-0196).

## References

1. D. Burr, et al., *J. Bone Min. Res.*, **12**, 6 (1997).
2. H. Leng, et al., *Biomaterials*, submitted.
3. X. Wang, et al., *J. Biomechanics*, submitted.
4. H. Leng, et al., *Ceram. Trans.*, **159**, 219 (2005).
5. J. Eastoe, et al., *Curr. Opin. Colloid Interface Sci.*, **1**, 800 (1996).
6. B. Niemann, et al., *Chem. Eng. Proc.*, **45**, 917 (2006).
7. L. Qi, et al., *Colloids Surfaces A: Physicochem. Eng. Aspects*, **108**, 117 (1996).
8. J. Koetz, et al., *Colloids Surfaces A: Physicochem. Eng. Aspects*, **250**, 423 (2004).
9. N.L. Ivanova, et al., *Colloid J.*, **63**, 786 (2000).
10. J.D. Hopwood, et al., *Chem. Mater.*, **9**, 1819 (1997).
11. D. Han, et al., *Powd. Technol.*, **147**, 113 (2004).
12. Z. Amjad, *Water Treatment*, **9**, 47 (1994).
13. Z. Jia, et al., *J. Colloid Interface Sci.*, **266**, 322 (2003).
14. M. Zhao, et al., *Nature Med.*, **7**, 1241 (2001).
15. R.C. Mehrotra, et al., Academic Press, New York, 1993.

# APS General User Proposal

**Proposal Title:** The detection limit of gold nanoparticles in x-ray tomography **GUP Id :** 8931

**Proposal Type:** Regular Proposal **Subject(s):** Materials science, Medical applications, Biological and life sciences, Engineering

**Status:** NEW

**Date Submitted:** **Review Panel:** Imaging/Microbeam

**Attached Files:**

**Required Techniques:** Tomography, Imaging: X-ray fluorescence

**Macromolecular crystallography ?N**

**Proprietary ?N**

**Classified ?N**

**Human subjects / materials ?N**

**Live animals ?N**

**Known Safety Hazard ?N**

**Funding:** DOD (specify), CDMRP & PRMRP through the US Army

## Scheduling

**Total Shifts Requested (Proposal):** 2

Rapid Access **Scheduling Period:** 2007-3 **Beamline:** First Choice: 13-BM-GSECARS  
**Requested Shifts:** 2 Second Choice: 2-BM-XOR  
**Requested Min Shifts:** 1

**Scheduling Requirements:** As soon as possible. A student will be commuting by a 3 hour drive.

**Equipment Requirements:** x-ray tomography and fluorescence tomography

We will bring no equipment with us.

**Unacceptable Dates:** From: 12/03/2007 To: 12/21/2007  
 From: 01/03/2008 To:

**Proposal Progress:** Samples were sent to Mark Rivers, who attempted some preliminary  
**Publications :** imaging. These experiments determined that our damage labeled with the nanoparticles was below the detection limit. Therefore, this proposal is aimed at determining the detection limit.  
 None. We are a new user. This proposal is for data to include in publications.

## Experimenters

**Name:** Ryan Roeder Spokesperson  
**Institution:** University of Notre Dame  
**Phone:** 574-631-7003  
**E-Mail:** rroeder@nd.edu

**Name:** \*Ryan Ross  
**Institution:** University of Notre Dame  
**Phone:** 574-631-1899  
**E-Mail:** rross@nd.edu

**Name:** Zhenyuan (Mark) Zhang  
**Institution:** University of Notre Dame  
**Phone:** 574-631-1898  
**E-Mail:** Zhenyuan.Zhang.48@nd.edu

\* Denotes an experimenter who will be on-site at the APS

# APS General User Proposal

## Abstract

**Proposal Title:** The detection limit of gold nanoparticles in x-ray tomography

Accumulation of microdamage in bone tissue can lead to an increased risk of fracture, including stress fractures in active individuals and fragility fractures in the elderly. Current methods for detecting microdamage are inherently invasive, destructive, tedious and two-dimensional. These limitations inhibit evaluating the effects of microdamage on whole bone strength and prohibit detecting microdamage in vivo. Therefore, we are investigating novel methods for detecting microdamage in bone using micro-computed tomography (micro-CT) and contrast agents with higher x-ray attenuation than bone. For proof-of-concept, the presence, spatial variation and accumulation of microdamage in cortical and trabecular bone specimens was nondestructively detected using micro-CT after staining with either lead sulfide or barium sulfate. However, specimens were stained in vitro via a precipitation reaction which was non-specific to damage and not biocompatible. Therefore, we are currently investigating the synthesis and functionalization of gold and barium sulfate nanoparticles for deliverable and damage-specific contrast agents. Unfortunately, commercial micro-CT scanners have been unable to detect the presence of these nanoparticles in damaged bone due to the small size and low concentration. Therefore, the objective of this proposal is to use synchrotron radiation to detect the presence of functionized gold nanoparticles 1) deposited in varying concentration in holes machined within a material (aluminum) with similar x-ray attenuation as cortical bone and 2) deposited in multiple monolayers on glass slides.

## Purpose and importance of research.

Accumulation of microdamage in bone tissue can lead to an increased risk of fracture, including stress fractures in active individuals and fragility fractures in the elderly. Current methods for detecting microdamage are inherently invasive, destructive, tedious and two-dimensional. These limitations inhibit evaluating the effects of microdamage on whole bone strength and prohibit detecting microdamage in vivo. Therefore, we are investigating novel methods for detecting microdamage in bone using micro-computed tomography (micro-CT) and contrast agents with higher x-ray attenuation than bone. For proof-of-concept, the presence, spatial variation and accumulation of microdamage in cortical and trabecular bone specimens was nondestructively detected using micro-CT after staining with barium sulfate [1-3]. However, specimens were stained in vitro via a precipitation reaction which was non-specific to damage and not biocompatible. Therefore, we are currently investigating the synthesis and functionalization of gold and barium sulfate nanoparticles for deliverable and damage-specific contrast agents [4-6]. Unfortunately, commercial micro-CT scanners have been unable to detect the presence of these nanoparticles in damaged bone due to the small size and low concentration. Therefore, the objective of this proposal is to use synchrotron radiation to detect the presence of functionized gold nanoparticles 1) deposited in varying concentration in holes machined within a material (aluminum) with similar x-ray attenuation as cortical bone and 2) deposited in multiple monolayers on glass slides.

## Reason for APS.

We have been unable to detect presence of our functionalized gold nanoparticle contrast agent within damaged bone using a commercial micro-CT scanner (Scanco micro-CT 80) due to the necessarily small size and low concentration. The use of synchrotron radiation is expected to provide higher resolution and sensitivity than we have available in our lab. We would also like to explore the use of fluorescence tomography.

## Reason for beamline choice.

Mark Rivers and Francesco DeCarlo have been very helpful with my questions and in facilitating some preliminary measurements.

## Previous experience with synchrotron radiation and results.

None. We are a new user. This proposal is for data to include in planned publications.

# APS General User Proposal

## Description of experiment(s).

Three experiments will be conducted:

1) Tomography on two, approximately 3 x 4 x 20 mm blocks of aluminum with 5 holes (2.4 mm diameter and 2.8 mm deep) along the length containing varying amounts/concentrations (100, 200, 300, 400 and 500  $\mu$ l of 0.5 mM Au NP colloid) of gold nanoparticles deposited in the holes.

2) Radiography and tomography of three, approximately 200  $\mu$ m x 2 x 20 mm glass slides with a varying number of gold nanoparticle monolayers deposited on one surface.

3) If we are unable to detect the gold nanoparticles in experiments 1 and 2, we would like to explore the use of fluorescence tomography on the same specimens (single slices). If we are able to detect the gold nanoparticles in experiments 1 and 2, we would still like to explore the use of fluorescence tomography but on the previous specimens where scratched surface damage labeled with gold nanoparticles was not able to be detected with conventional tomography.

## Estimated amount of beam time, number of visits, number of shifts. (approximately)

Per discussion with Mark Rivers, two 8 hours beam shifts should be sufficient to perform the aforementioned measurements. The two shifts should probably be scheduled at different times, such that data from experiments 1 and 2 can be analyzed prior to exploring experiment 3.

## References

1. H. Leng, X. Wang, R.D. Ross, G.L. Niebur and R.K. Roeder, "Micro-Computed Tomography of Fatigue Microdamage in Cortical Bone Using a Barium Sulfate Contrast Agent," J. Mech. Behav. Biomed. Mater., 1 [1] 68-75 (2008).
2. X. Wang, D.B. Masse, H. Leng, K.P. Hess, R.D. Ross, R.K. Roeder and G.L. Niebur, "Detection of trabecular bone microdamage by micro-computed tomography," J. Biomechanics, in press.
3. H. Leng, X. Wang, G.L. Niebur and R.K. Roeder, "Fatigue Microdamage in Bovine Cortical Bone Imaged by Micro-Computed Tomography Using a Barium Sulfate Contrast Agent," Mater. Res. Soc. Symp. Proc., 898E, L09-04 (2005).
4. Z. Zhang, R.D. Ross and R.K. Roeder, "Functionalized Gold Nanoparticles as a Damage Specific Contrast Agent for Bone," Trans. of the 33rd Annual Meeting of the Society for Biomaterials, Chicago, IL, 30, 93 (2007).
5. M.J. Meagher, Z. Zhang, and R.K. Roeder, "Precipitation of a Barium Sulfate Nanoparticle Contrast Agent Using Microemulsions," 2007 TMS Annual Meeting, Orlando, FL (2007).
6. H. Leng, X. Wang, G.L. Niebur and R.K. Roeder, "Synthesis of a Barium Sulfate Nanoparticle Contrast Agent for Micro-Computed Tomography of Bone Microstructure," Ceram. Trans., 159, 219-229 (2004).